Materials Today • Volume xxx, Number xx • xxxx 2023

ELSEVIER

Piezo-phototronic and pyro-phototronic effects enhanced broadband photosensing

Shuo Tian [a], Bin Li [a], Yejing Dai [a,*], Zhong Lin Wang [b,c,d,*]

[a] School of Materials, Shenzhen Campus, Sun Yat-sen University, Shenzhen 518107, PR China
[b] Beijing Institute of Nanoenergy and Nanosystems, Chinese Academy of Sciences, Beijing 100083, PR China
[c] School of Materials Science and Engineering, Georgia Institute of Technology, Atlanta, GA 30332-0245, USA
[d] Yonsei Frontier Lab, Yonsei University, Seoul 03722, Republic of Korea

The piezoelectricity and pyroelectricity of third-generation semiconductor materials (such as ZnO, GaN, and CdS) distinguish them from traditional semiconductors and give rise to two novel effects: the piezo-phototronic effect and the pyro-phototronic effect. The piezo-phototronic effect is to use the piezoelectric polarization charges at the heterointerface to tune the electron-hole separation or recombination in optoelectronic processes. For the pulsed incident light, local generated heating results in a strong pyroelectric effect, which gives a high output voltage and current. This is the pyro-phototronic effect. In this review, we give a systematic introduction to the two effects. Following that, recent advances in piezo-phototronic and pyro-phototronic effects enhanced broadband photosensing, including applications of the piezo-phototronic and pyro-phototronic effects in broadband photodetectors and their synergy effect, are thoroughly summarized. Finally, a perspective is given regarding their future impacts.

Keywords: Piezo-phototronics; Pyro-phototronics; Broadband photosensing; Photodetector

Introduction

Over the past three decades, the fabrication and creation of nanomaterials, as well as research in related fields of technology, have advanced quickly. This has made them a hot topic in international science and technology fields, with numerous potential applications in the fields of communications, environment, energy, materials, chemistry, microelectronics, biology, medicine, and other fields [1–7]. It is worth noting that the heterojunction interface possesses important physical properties and plays a significant role in the performance of nano-(opto) electronic devices [8–12]. Therefore, the modulation of interface properties is crucial for the construction of new functional nanodevices and the optimization of device performance [13–15].

Based on piezoelectric semiconductor materials, such as ZnO [16–18], GaN [19,20], InN [21] and CdS [22–25] known as third-generation semiconductor materials [26], two whole new fields of research, namely piezo-phototronics and pyro-phototronics by coupling piezoelectricity/pyroelectricity, semiconductor property, and photoexcitation, have been proposed by Z. L. Wang in 2010 [27–29] and 2015 [13,30,31], respectively. The piezoelectric polarization charges (piezocharges) or pyroelectric polarization charges (pyrocharges) arising from the strain or temperature change can modulate the energy band structure at the interface of the heterojunction, thereby effectively controlling the generation, separation, transport, and recombination behavior of photogenerated carriers at the interface [3,13]. The piezo-phototronic and pyro-phototronic effects, which have been applied to various types of heterojunction devices, have opened up new avenues for optimizing device performance (Fig. 1) [32,33].

* Corresponding authors at: Beijing Institute of Nanoenergy and Nanosystems, Chinese Academy of Sciences, Beijing 100083, PR China (Z.L. Wang).

E-mail addresses: Dai, Y. (daiyj8@mail.sysu.edu.cn), Wang, Z.L. (zhong.wang@mse.gatech.edu).

1369-7021/© 2023 Elsevier Ltd. All rights reserved. https://doi.org/10.1016/j.mattod.2023.07.001

Please cite this article in press as: S. Tian et al., Materials Today, (2023), https://doi.org/10.1016/j.mattod.2023.07.001

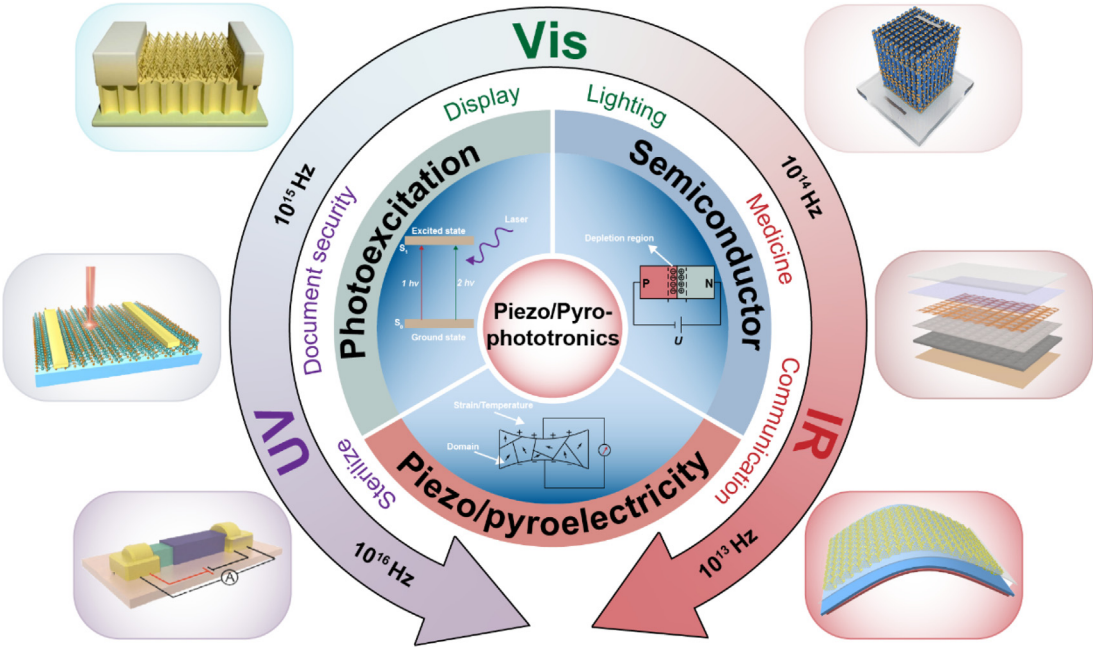

FIG. 1

Schematic illustrations of the piezo-phototronic and pyro-phototronic effects enhanced broadband photosensing for different device structures.

In recent years, it has been demonstrated that the piezo-phototronic and pyro-phototronic effects play an important role in solar cells, light-emitting diodes (LEDs), photocatalysis, and, most notably, photodetectors [34–37]. Although there is a growing demand for photodetectors, it remains difficult to achieve broadband response with high sensitivity, fast response times, and good stability, which is conducive to optical communication, modern multispectral detection, and environmental surveillance [38–41]. The piezo-phototronics and pyro-phototronics have been confirmed to improve these aspects significantly by directly modulating the energy band structure at the interface through strain or temperature changes, which is difficult to achieve for photodetectors with traditional technology. Here, we provide a comprehensive review of state-of-the-art research on the piezo-phototronic and pyro-phototronic effects enhanced broadband photosensing with various device structures. Then, coupling the pyro-phototronic effect with other effects is also summarized and discussed here. Finally, the future research challenges and outlook are discussed. This review provides an in-depth understanding of the piezo-phototronic and pyro-phototronic effects, as well as an insightful outlook on them.

Fundamentals of the piezo/pyro-phototronic effect

Piezoelectric potential and pyroelectric potential

The core of the piezo-phototronic and pyro-phototronic effects is the piezoelectric potential and pyroelectric potential generated in piezoelectric semiconductor materials, thereby possessing simultaneously piezoelectricity/pyroelectricity, semiconductor, and photoexcitation property [33,42]. Compared with conventional semiconductors, the most notable feature of third-generation semiconductor materials, such as ZnO, GaN, and CdS with wurtzite structure [29,43–45], is their piezoelectricity and pyroelectricity [46]. Wurtzite structural crystals with a hexagonal structure have a significant anisotropy along and perpendicular to the *c*-axis. Taking ZnO as an example [3], it has a non-centrosymmetric crystal structure and exhibits a piezoelectric effect when deformed under applied stress (Fig. 2a). The Zn^{2+} cation and the adjacent O^{2-} anions form a regular tetrahedron structure with the cation as the center. As shown in Fig. 2b, in the absence of external stress, the charge centers of cation and anions overlap with each other and are macroscopically uncharged. When stress is applied to the apex of the regular tetrahedron, the charge centers of the cation and anions are displaced relative to each other, resulting in a dipole moment. The superposition of the dipole moments generated by all the cells in the crystal produces a macroscopic potential distribution along the stress direction, which is the piezoelectric potential [47,48] (Fig. 2c). When the stress is applied, the piezoelectric potential generated in the piezoelectric material can drive electrons to flow into the external circuit load, forming the piezoelectric current [3]. Similarly, the pyroelectric potential along a specific direction in the crystal can be generated as a result of the charge center displacement of the cation and anions caused by the change in temperature [49]. The pyroelectric current can be expressed as $I_p = pA(dT/dt)$, where p and A are the pyroelectric coefficient and the electrode area, respectively. It is clear that the pyroelectric current can be increased by increasing the temperature variation rate [50]. Based on this, detectors based on the pyroelectric effect are capable of detecting a wide range of wavelengths, from the visible (Vis) to the infrared region, which is conducive to broadband and fast photosensing. Actually, the piezoelectric potential and the pyroelectric potential are essentially the same, that is, a

Please cite this article in press as: S. Tian et al., Materials Today, (2023), https://doi.org/10.1016/j.mattod.2023.07.001

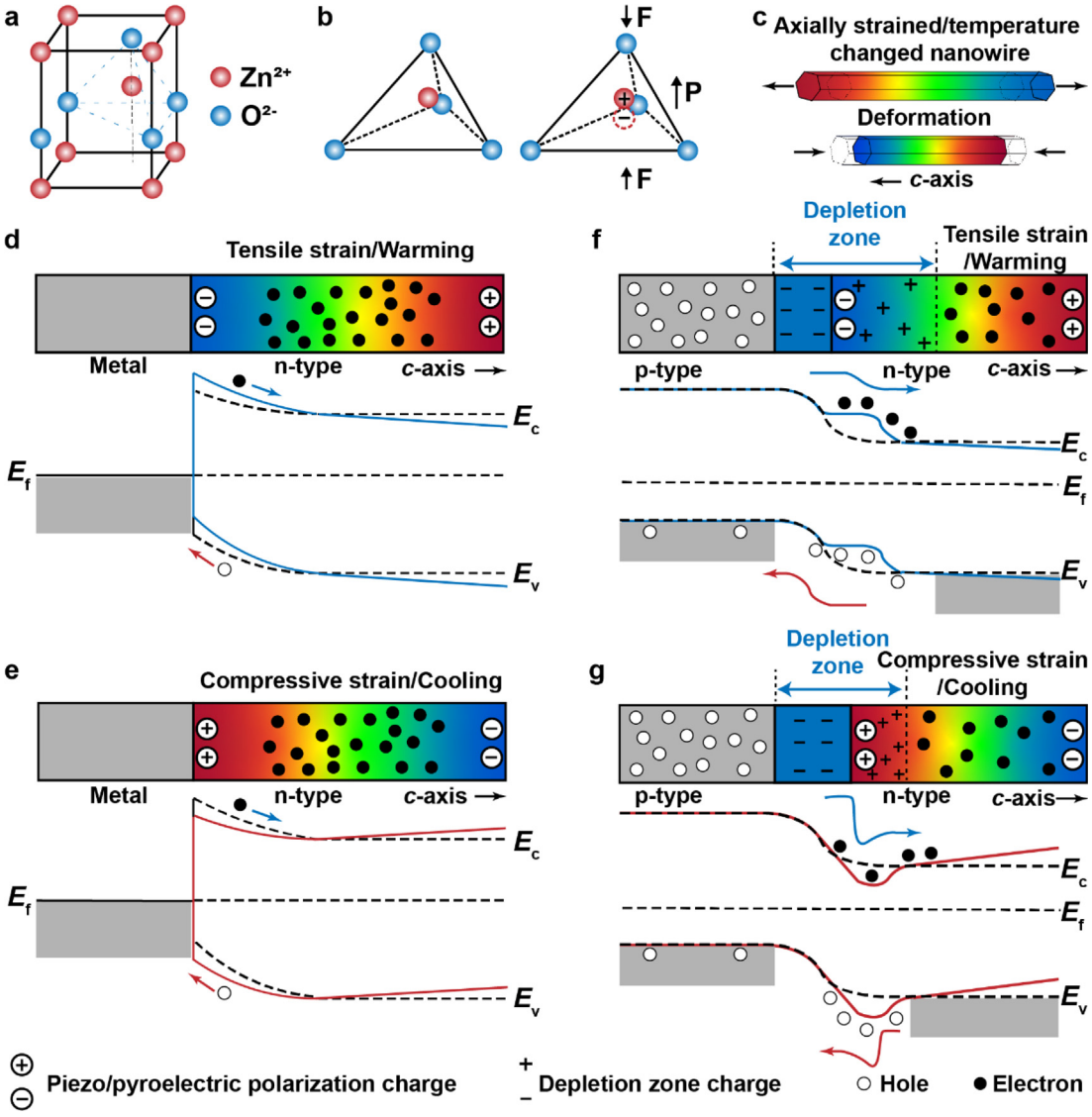

FIG. 2

Piezoelectric and pyroelectric potential in ZnO wurtzite crystal and the energy band diagram for illustrating the piezo-phototronic and pyro-phototronic effects. (a, b) Atomic model of wurtzite-structured ZnO. (c) Piezoelectric and pyroelectric potential distributed along the c-axis in a ZnO nanowire under the strain or temperature change. (d, e) Band diagrams of the metal–semiconductor contact for the piezo-phototronic and pyro-phototronic effects. (f, g) Band diagrams of the p-n junction for the piezo-phototronic and pyro-phototronic effects. Reproduced with permission [3]. Copyright 2012, Wiley-VCH.

change in volume due to stress or temperature causes a change in the dipole moment. The piezoelectric and pyroelectric potentials in semiconductor materials are the basis of the piezo/pyro-phototronic effect.

Effect of piezo/pyroelectric potential on metal–semiconductor (M−S) contact

The metal–semiconductor contact is a representative heterojunction for the electronic devices. When a metal is in contact with an n-type semiconductor, a Schottky barrier (SB) is formed at the metal–semiconductor junction interface if the work function of the metal material is higher than the electron affinity potential of the semiconductor material [51–53]. When under laser illumination, a built-in electric field generated by the Schottky contact can separate and collect electrons and holes, resulting in a photocurrent. Thus, the photocurrent can be tuned by modulating the Schottky barrier height (SBH) in the junction region [54–59].

For the piezo-phototronic effect, when a strain is applied along the *c*-axis direction of the piezoelectric semiconductor, the resulting negative piezoelectric charges at the semiconductor side of the interface can repel the electrons away from the M−S interface, leading to a wider depleted interface and an enhanced local SBH (Fig. 2d), while the resulting positive piezoelectric charges can attract the electrons toward the M−S interface, leading to a narrower depleted interface and a lower local SBH (Fig. 2e) [3]. Similarly, for the pyro-phototronic effect, the negative or positive piezoelectric charges can be regulated through the change in temperature of the pyroelectric material by turning on or off the laser. As we know, the polarity and magnitude of the piezoelectric potential and pyroelectric potential can be changed by changing the type (compression or tension) and

Please cite this article in press as: S. Tian et al., Materials Today, (2023), https://doi.org/10.1016/j.mattod.2023.07.001

magnitude of strain or the type (warming or cooling) and speed of the temperature change, and thus the SBH can be modulated by the strain and temperature. Consequently, the piezoelectric or pyroelectric effect, which can efficiently control the separation and transport process of charge carriers near the metal–semiconductor interface, can be used to vary the local band structure at the interface of a Schottky contact [30,31,60–62]. Such modulation is the fundamental mechanism of piezo/pyro-phototronics in a Schottky contact.

Effect of piezo/pyroelectric potential on p-n junction

The p-n junction is another representative heterostructure for current electronic devices. When a p-type semiconductor and an n-type semiconductor contact to form a p-n junction, the mutual diffusion and recombination processes of electrons and holes lead to the formation of a charge depletion region at the interface [63–65]. The photogenerated electrons and holes transport through the depletion region, leading to a photocurrent. Similarly, the piezoelectric and pyroelectric charges induced at the p-n junction interface also have an effect on the band structure [3].

Taking an n-type piezoelectric semiconductor material as an example, when a tensile strain is applied along the *c*-axis direction of the piezoelectric semiconductor, negative piezoelectric charges will be formed on the n-type side at the interface. Consequently, the negative piezoelectric charges would attract the holes toward the interface and repel the electrons away from the interface of the heterojunction, leading to an upward bending of the energy band based on Anderson's model and a shifting of the depletion region toward the n-type side (Fig. 2f) [66]. On the contrary, if compressive stress is applied to the piezoelectric semiconductor, positive charges will be formed on the n-type side at the interface. The positive piezoelectric charges would attract the electrons toward the interface and repel the holes away from the interface of the heterojunction, leading to a downward bending of the energy band and a shifting of the depletion region toward the p-type side (Fig. 2g). Similar discussions can also be easily deduced in other heterojunction cases. Therefore, both the strain and temperature can be utilized to effectively control the band structure, thus adjusting the generation, transport, separation, and recombination of photogenerated carriers near the p-n junction interface. This is the basic working mechanism of the piezo/pyro-phototronics based on the p-n junction.

Broadband photodetectors based on the piezo-phototronic effect

Single semiconductor nanowire structure

With a direct bandgap of 1.44 eV at room temperature, CdTe, a group II–VI semiconductor, is prominent for many optoelectronic applications in the visible spectrum [67,68]. Introducing the piezo-phototronic effect to the photodetector can improve its photoresponse behavior [69]. CdTe nanowires (NWs) are transferred from the silicon wafer onto the polyethylene terephthalate (PET) substrate with two Ag electrodes at the ends of the NWs. The CdTe layer is encapsulated in polymethyl methacrylate (PMMA), and the electrodes are led out with wires, as shown in Fig. 3a. Fig. 3b is the X-ray diffraction (XRD) pattern of CdTe. It can be seen that CdTe is successfully synthesized with a high-crystalline structure. Fig. 3c1-c3 shows the *I-V* curves of the photodetector illuminated at different wavelengths and power densities of light, indicating the broadband photosensing ability. The photoresponse under different strains is further investigated to demonstrate the influence of the piezo-phototronic effect (Fig. 3d). With increasing compresive strain, the photocurrent increases significantly. However, the photocurrent decreases with increasing threshold voltage when the strain exceeds 0.66%. This is due to the fact that the photocurrent and the performance of the photodetector are both impacted by two competing processes when the compressive strain is applied to the NW. The reduction in the SBH induced by piezo-phototronics will make it easier for photogenerated carriers to be transported, which will increase the photocurrent. The drop in SBH causes a shortening of the interface depletion layer as the compressive strain increases, which weakens the built-in electric field and reduces the photocurrent. The two processes compete with each other, thus when the compressive strain increases, an optimized value rather than a monotonous change of the photocurrent is generated.

Nanorod array/conductive films structure

Broadband photodetection from the ultraviolet (UV) to infrared bands is still a great challenge. Semiconductors with a narrow band gap are promising for photodetection in the infrared band. However, there are two major limitations for conventional narrow-bandgap semiconductors in the infrared band: one is that there are few type-Ⅱ heterojunctions to match them, and the other is that the large dark current deteriorates their photoresponse ability [70,71]. In recent years, researchers have found that the Schottky junctions between reduced graphene oxide (rGO) and semiconductors have good photoresponse under high-frequency illumination [72,73]. Besides, the band gap and work function of rGO can be controlled by the degree of reduction, and the light absorption degree can be easily controlled by the thickness of the film [72]. Thus, a narrow bandgap rGO compounded with a wide bandgap semiconductor can form a broadband heterojunction [74]. Fig. 4a shows the fabrication process of the CdS nanorod (NR) array/rGO film Schottky junction photodetector. Firstly, CdS NR arrays are grown on a fluorine-doped tin oxide (FTO) substrate using the hydrothermal method, and a layer of graphene oxide is spin-coated on top to form a heterojunction. Then, the graphene layer is reduced to reduced graphene oxide in a hydrogen atmosphere, and finally, silver paste and carbon paste are coated on both sides as top and bottom electrodes. Fig. 4b shows a comparison of the photodetector under dark and UV illuminations, indicating the presence of the photovoltaic effect. In Fig. 4c, the photocurrent of the photodetector increases with the light intensity at zero bias voltage, demonstrating its excellent self-powered photoresponse. The photodetector has a fast response time with a rise time (T_r) of 1.3 ms and a decay time (T_d) of 1.7 ms (Fig. 4d). When the device is illuminated at different wavelengths, it displays excellent photoresponse characteristics (Fig. 4e), indicating its promising application in the field of broadband photosensing. Fig. 4f shows the photocurrent of the photodetector under different strains.

Please cite this article in press as: S. Tian et al., Materials Today, (2023), https://doi.org/10.1016/j.mattod.2023.07.001

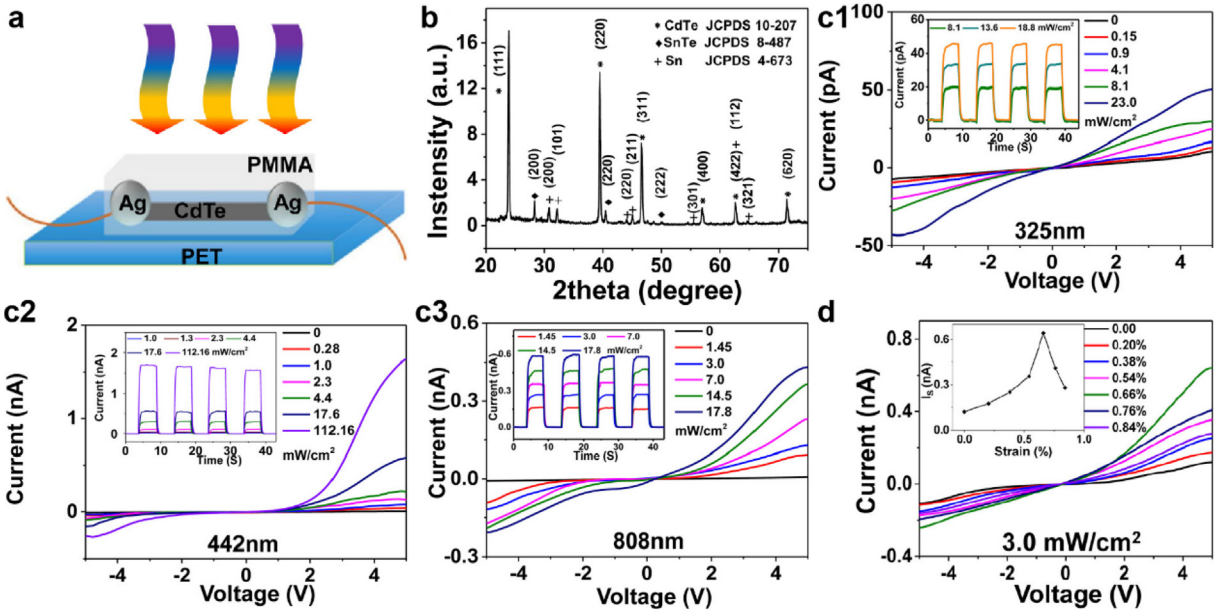

FIG. 3

Single CdTe nanowire. (a) Schematic diagram of the single CdTe nanowire photodetector. (b) XRD pattern of CdTe. *I-V* characteristics with various power densities at (c1) 325 nm, (c2) 442 nm, and (c3) 808 nm laser illuminations. (d) *I-V* characteristics under different compressive strains at 808 nm laser illumination. Reproduced with permission [69]. Copyright 2018, American Institute of Physics.

The maximum current reaches 780 nA as the strain increases from 0% to −0.4%. Fig. 4g reveals the effect of compressive strain on the Schottky junction using an energy band diagram. The negative piezoelectric potential at the interface raises the local energy band height of CdS, and the increase in the SBH and the width of the depletion region on the CdS side promote the separation and extraction of photogenerated carriers, which improve the photocurrent and photoresponse.

Core-Shell structure

Photodetectors with core–shell structures have many advantages, such as large contact areas, multi-channel charge transport, and enhanced light absorption by light trapping and scattering [75–78]. The core–shell nanowire structure also can enhance the carrier lifetime by separating electrons and holes in different conducting channels [79,80], inhibit their recombination and scatter losses, and improve quantum efficiency [81–85], which significantly enhances the broadband photodetection response [86]. In addition, the core–shell structure of the photodetector can be processed into various shapes, even making the device flexible [87]. Since CdSe and ZnTe are ideal core–shell structure constituents due to the small lattice mismatch, similar thermal expansion coefficients, and type-Ⅱ band alignment [88], they achieved good photoresponse in the UV–visible wavelength range in combination with the piezo-phototronic effect [89]. Further, if ZnTe is replaced by CdTe as the shell layer, the response band can be extended to the near-infrared (NIR) range [90]. Fig. 5a shows the fabrication process of the CdSe/CdTe core–shell nanowire array. A 100-nm-thick CdSe film is first deposited on mica, and a 3-nm-thick layer of gold is coated as a catalyst for nanowire growth. The CdSe nanowire arrays are then grown by chemical vapor deposition (CVD). Epitaxial growth of the CdTe layer on the surface of CdSe is achieved using pulsed laser deposition (PLD) to form a core–shell structure, and silver paste is applied on top as the top electrode. Fig. 5b shows the performance of the photodetector under different compressive loads and bias voltages with different light illuminations. The photodetector presents a good response to different wavelengths of laser, and the peak current increases gradually with increased compressive strain. Due to the indirect type-II transition of electrons between the valence band maximum of the CdTe (shell) and the conduction band minimum of the CdSe (core) in a core–shell nanowire, even in the NIR band, the photocurrent remains at the milliamp level. Fig. 5c shows the variation of photocurrent under different compressive loads, showing a gradual increase, which demonstrates the positive impact of the piezo-phototronic effect in broadband photoresponse. The band diagram of the CdSe/CdTe interface under a compressive strain is illustrated in Fig. 5d. The local negative polarization charges caused by the compression strain in the CdSe side make the edges of valence band and conduction band bend upward, resulting in a rapid separation of holes and electrons and an increase in peak photocurrent.

p-intrinsic-n junction structure

In recent years, it has been found that carrier separation and collection efficiency can be greatly improved if an insulating layer is added between the p-type and n-type materials, compared to the conventional p-n junction structure [91]. Instead of the conventional p-insulation-n strategy, a 15-nm-thick alumina insulator layer was added between p-type Si and n-type ZnO [92]. A dual inversion layer in the depletion zone is successfully established, and the photogenerated carriers can pass through the alumina insulator layer in a controlled manner through the quantum mechanical Fowler-Nordheim tunneling mechanism, resulting in a significant increase in photoresponse and sensitivity. How-

Please cite this article in press as: S. Tian et al., Materials Today, (2023), https://doi.org/10.1016/j.mattod.2023.07.001

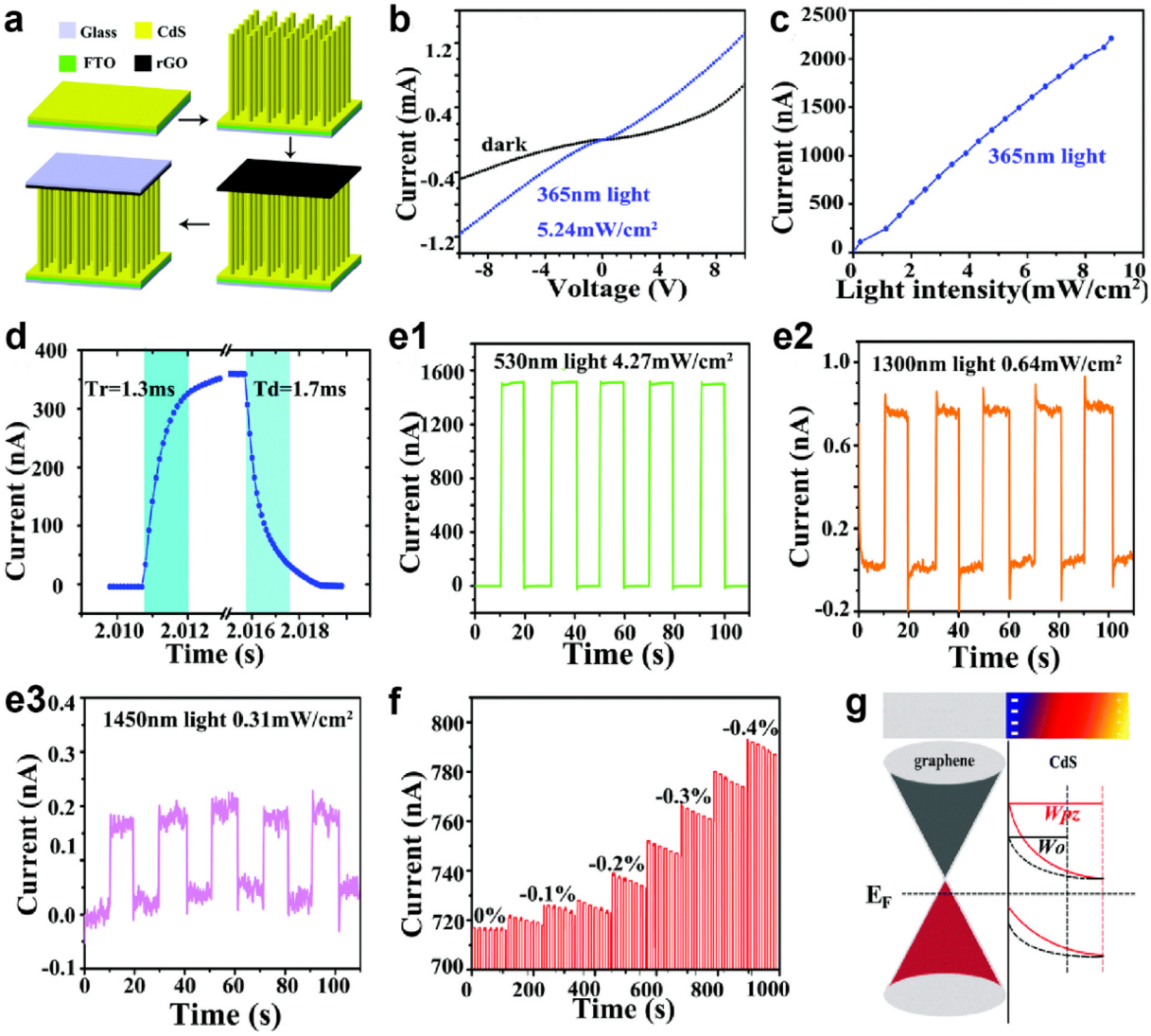

FIG. 4

CdS NR array/rGO film photodetector. (a) Fabrication process of the photodetector. (b) *I-V* curves of the CdS NR array/rGO photodetector under dark and 365 nm light illuminations. (c) Photocurrent of the photodetector versus the light intensity under UV illumination at zero bias. (d) Response time of the photodetector in one cycle. (e1-e3) *I-t* curves of the photodetector under different light illuminations. (f) Photocurrent at a power density of 3.2 mW cm^{-2} under different compressive strains. (g) Band diagram of the CdS/rGO interface under a compressive strain. Reproduced with permission [74]. Copyright 2018, Royal Society of Chemistry.

ever, the indirect energy band and large surface reflection limit the light absorption of silicon-based optoelectronic devices, especially for near-infrared light with wavelengths greater than 900 nm. Thus, a textured top ceiling electrode is designed to enhance the absorption of NIR light. Fig. 6a is a schematic diagram of the three-dimensional structure of the device. First, a 15-nm-thick AlO_x layer is coated to the Si substrate using atomic layer deposition (ALD), and then a uniform array with a thickness of 70–80 nm and a length of 2 μm ZnO NWs is grown on the insulator layer. Indium tin oxide (ITO) and aluminum are used as the top and bottom electrodes of the device, respectively. Fig. 6b shows the absorption of p-Si/AlO_x/n-ZnO, p-Si, and n-ZnO for different wavelengths. As mentioned above, the absorption of p-Si for wavelengths greater than 900 nm decreases, but the p-Si/AlO_x/n-ZnO can still maintain a high absorption for the spectrum above 900 nm, which benefits from the specially designed textured top ceiling electrode. The variation of photocurrent with different power densities at 442 nm and 1060 nm wavelengths is shown in Fig. 6c, d. The addition of the AlO_x layer results in a significant increase in photocurrent, and there is no saturation of the photocurrent with increasing power density compared to that without the AlO_x layer. The sensitivity of the p-Si/AlO_x/n-ZnO diode is 12.4 and 8.9 times larger than that of the device without an AlO_x layer under illuminations of 442 nm (Fig. 6e) and 1060 nm (Fig. 6f), respectively, which indicates that the insulator layer can effectively enhance the carrier separation. The responsivity increases with the power density without reaching saturation (Fig. 6g). When the power density increases, the shift in the Fermi energy level and energy band causes more carriers to appear in the dual inversion layer at the interface, resulting in enhanced current collection capability in this region. A systematic investigation of the piezo-

Please cite this article in press as: S. Tian et al., Materials Today, (2023), https://doi.org/10.1016/j.mattod.2023.07.001

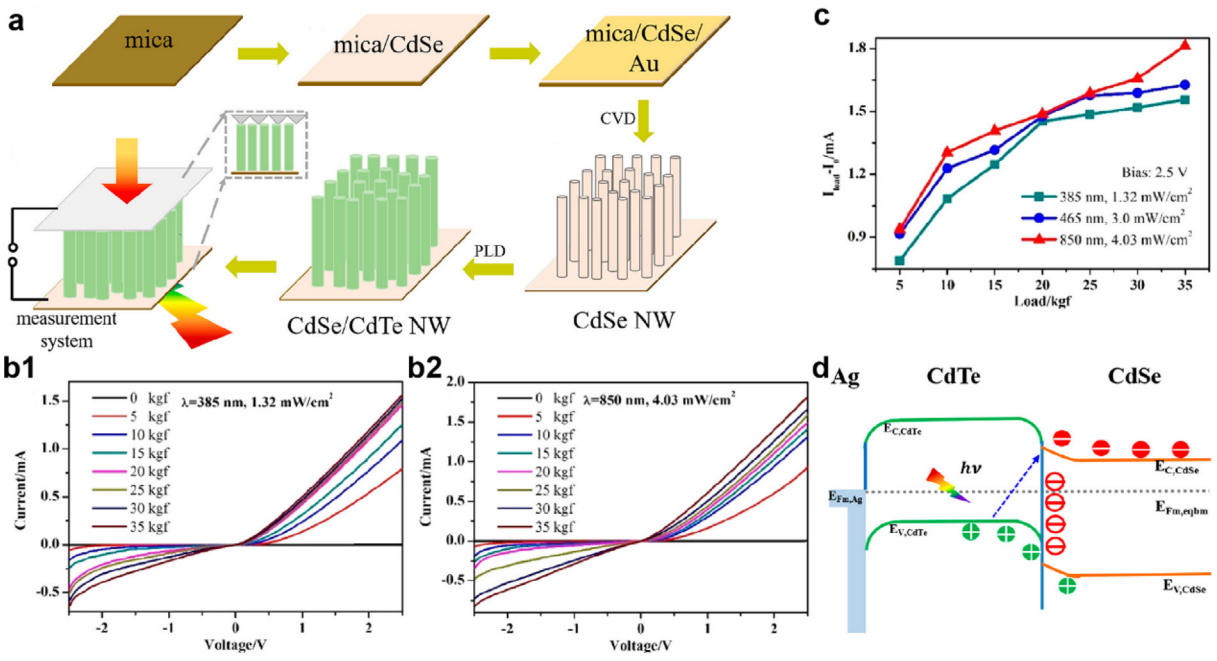

FIG. 5

CdSe/CdTe core–shell nanowire array. (a) Fabrication process of the CdSe/CdTe core–shell nanowire array. (b1, b2) *I-V* curves for the CdSe/CdTe core/shell array photodetector under different compressive loads and wavelength illuminations. (c) Absolute current of the photodetector under different compressive loads at 385 nm, 465 nm, and 850 nm light illuminations. (d) Band diagram of the CdSe/CdTe interface under a compressive strain. Reproduced with permission [90]. Copyright 2020, American Chemical Society.

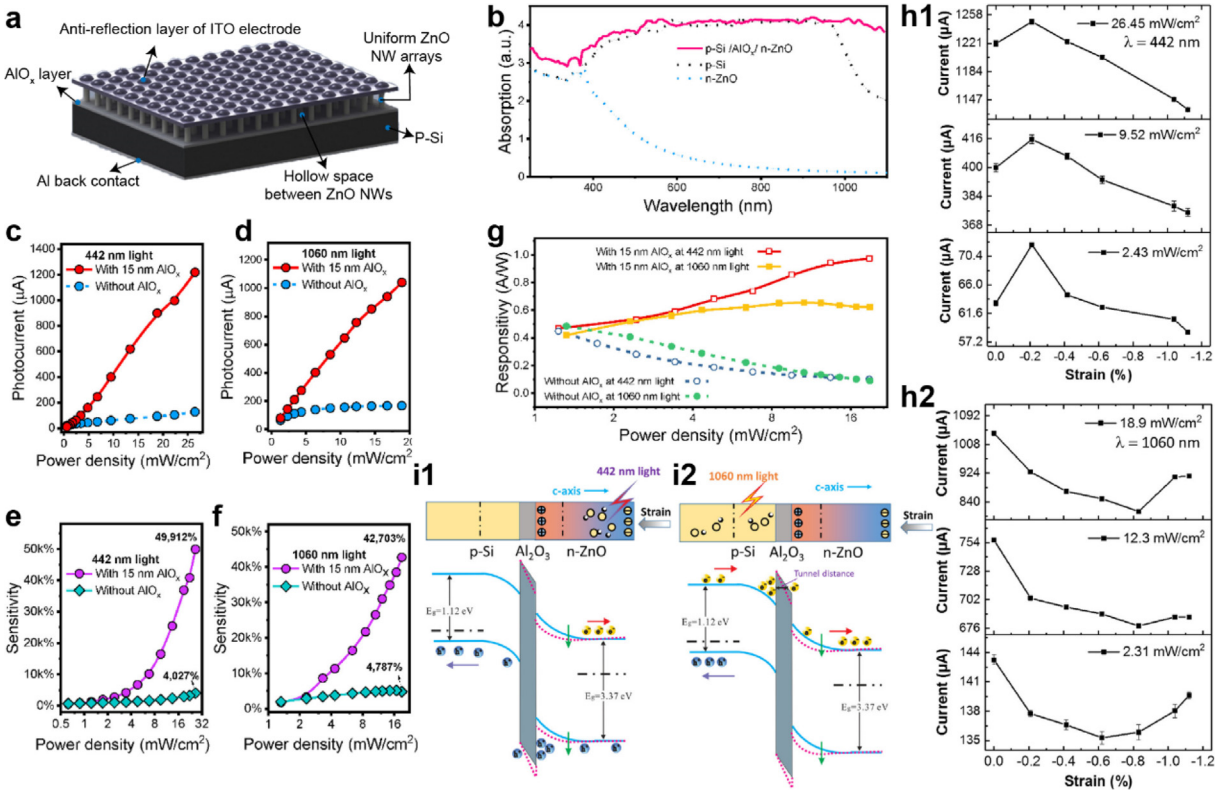

FIG. 6

A p-Si/AlO_x/n-ZnO NW array photodetector. (a) Structure design of the photodetector. (b) Absorption spectra of p-Si, n-ZnO, and the p-Si/AlO_x/n-ZnO device. Photocurrent of the device with different power densities under (c) 442 nm and (d) 1060 nm illuminations. Sensitivity of the device with different power densities under (e) 442 nm and (f) 1060 nm illuminations. (g) Responsivity of the devices with various power densities of 442 nm and 1060 nm illuminations. Output current with different strains and power densities at a −2 V bias under (h1) 442 nm and (h2) 1060 nm illuminations. (i) Band diagram of the p-Si/AlO_x/n-ZnO NW array. Reproduced with permission [92]. Copyright 2019, American Chemical Society.

Please cite this article in press as: S. Tian et al., Materials Today, (2023), https://doi.org/10.1016/j.mattod.2023.07.001

phototronic effect was carried out. Interestingly, for 442 nm and 1060 nm wavelengths, there is an opposite phenomenon, as shown in Fig. 6h. This phenomenon is clearly explained in Fig. 6i. For the 442 nm spectrum, the positive piezoelectric potential in the inversion layer on the ZnO side will lead to a local increase in charge density, resulting in a strong built-in electric field and an increase in charge separation and collection. When the strain is further increased, the piezoelectric potential will bend the energy bands of ZnO and AlO_x downward, and the charge will accumulate on the side of AlO_x, suppressing the charge separation and collection efficiency. For the 1060 nm spectrum, the piezoelectric potential also shortens the tunnel distance for tunneling. The charge density on the Si side is lowered, and the effect of the inversion layer is weakened, making the photocurrent drop. However, when the strain further increases, the shortened tunneling distance will be small enough to make the carriers pass through the insulator layer directly without an effective inversion layer. The screening effect cannot compete with the piezo-phototronic effect, resulting in a boost in photocurrent.

Huo *et al*. used Al_2O_3 as an insulator layer to enhance the photoresponse performance of a p-ZnO NW-based UV–Vis-NIR photodetector, which achieved a fast response time [93]. The fabrication process is similar to p-Si/AlO_x/n-ZnO. The structure and fabrication process of n-Si/Al_2O_3/p-ZnO are shown in Fig. 7a. The difference is that ZnO is doped by Sb to form a p-type semiconductor. ZnO is generally an n-type semiconductor, and it is usually difficult to prepare reliable p-type ZnO for practical applications. Fig. 7b shows the absorption of n-Si/Al_2O_3/p-ZnO, n-Si/p-ZnO, n-Si, and p-ZnO for different wavelengths, which indicates that the intervention of the insulating Al_2O_3 layer makes the photodetector maintain excellent absorption above 900 nm. Fig. 7c illustrates the *I-V* curves of the photodetector in the dark environment and under various wavelengths of the spectrum. Excellent response in the UV, visible, and NIR bands means that the n-Si/Al_2O_3/p-ZnO photodetector has broadband photoresponse characteristics and shows better response at reverse bias than at forward bias. The sensitivity of the photodetector with and without an Al_2O_3 layer at different power densities from UV to NIR is plotted in Fig. 7d. By introducing the insulator layer, the sensitivity of the photodetector is greatly enhanced. The sensitivity of the photodetector with an 8 nm Al_2O_3 layer reaches 50000% under 325 nm illumination, 22000% under 633 nm illumination, and 31000% under 1064 nm illumination, respectively. It is worth mentioning that this photodetector has a fast photoresponse (Fig. 7e), and the rise time and fall time under UV, visible, and NIR are 180/230, 130/70, and 140/180 μs, respectively, which demonstrates excellent photoresponse performance in the UV–Vis-NIR broadband. The responsivity *R* and specific detectivity *D** with the piezo-phototronic effect are systematically analyzed, and the results under visible light are shown in Fig. 7f. Under UV illumination, the *R* and *D** reach 13.80 A W^{-1} and 3.12 × 10^{12} Jones under 0.69 mW cm^{-2} of illumination and a −0.79‰ compressive

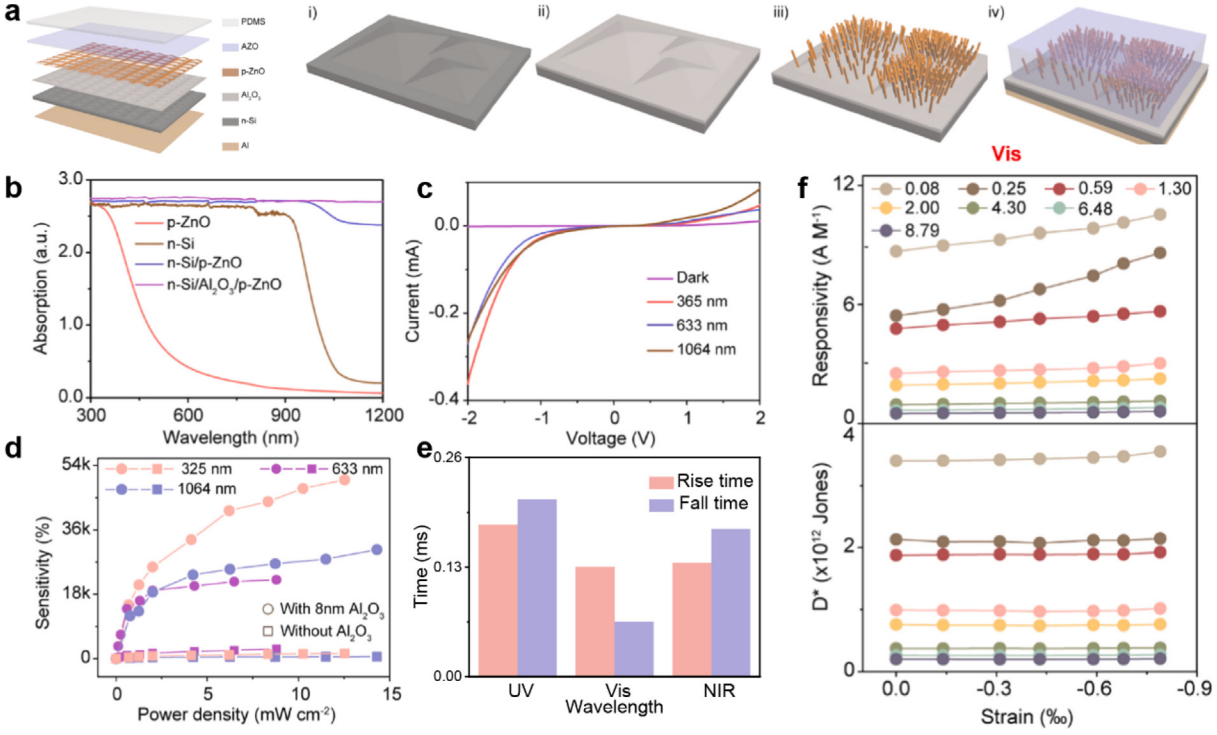

FIG. 7

A p-ZnO/Al_2O_3/n-Si heterojunction device. (a) Schematic illustration and fabrication process of the heterojunction. (b) Absorption spectra of p-ZnO, n-Si, p-ZnO/n-Si, and the p-ZnO/Al_2O_3/n-Si device. (c) *I-V* curves of the heterojunction under dark and various wavelengths of illumination with power densities of 2 mW cm^{-2}. (d) Sensitivity of the photodetector with or without the Al_2O_3 layer under 365 nm, 633 nm and 1064 nm light illuminations. (e) Response time of the photodetector under UV, visible, and NIR lights. (f) The responsivity and specific detectivity of the photodetector with different power densities and strains under visible light. Reproduced with permission [93]. Copyright 2021, Elsevier Ltd.

Please cite this article in press as: S. Tian et al., Materials Today, (2023), https://doi.org/10.1016/j.mattod.2023.07.001

strain. Under visible illumination, the two values reach 10.60 A W^{-1} and 3.55 × 10^{12} Jones under −0.79‰ strain with 0.08 mW cm^{-2}, respectively. The *R* and *D** reach 16.30 A W^{-1} and 2.70 × 10^{12} Jones under NIR illumination, respectively. These results reveal that the introduction of the insulator layer and the piezo-phototronic effect can significantly enhance the broadband photoresponse properties of p-n heterojunctions.

Organic/inorganic structure

Compared to inorganic photodetectors, organic/inorganic photodetectors are low-cost, flexible, and exhibit excellent adhesion, which have attracted wide attention [94–96]. 3-hexyl-substituted polythiophene (P3HT) is a typical p-type semiconductor with excellent stability, low cost, and easy chemical modification [97–99], and a CdS-P3HT organic/inorganic self-powered photodetector is fabricated [100]. Due to the good adhesion between P3HT and CdS microwire and the type-II band alignment, the photodetector exhibits excellent optoelectronic properties. Fig. 8a shows the structure of the device and measurement platform, and different tensile strains are controlled by different displacement distances at the free end. Fig. 8b shows the *I-V* curves of the device under different wavelengths of laser illumination with different intensities. The photodetector responds well to different wavelengths of laser illumination and displays a broadband photoresponse capability. The effect of positive and negative piezopotentials on the on–off current response at zero bias voltage is then investigated by applying compressive and tensile strains to the CdS-P3HT photodetector, as shown in Fig. 8c, d. When the CdS side at the interface possesses positive pizeopotential, the photocurrent gradually increases with increasing strain. However, when the pizeopotential at the interface is negative, the photocurrent is suppressed. This is because the positive pizeopotential at the interface raises the barrier height, while the negative pizeopotential lifts the local conduction band energy level and thus lowers the barrier height. Therefore, by introducing the piezo-phototronic effect into the CdS-P3HT self-powered photodetector, the photodetection performance of the devices can be modulated.

Broadband photodetectors based on the pyro-phototronic effect

p-Si/n-CdS nanowires heterostructure

CdS has been confirmed to be an excellent optoelectronic material due to extraordinary thermal and chemical stability [101–103]. However, a weak light absorption capacity limits the applications, which can be solved by combining it with other materials [104]. A p-Si/n-CdS NWs heterostructure with a broadband photoresponse from 325 nm to 1550 nm is fabricated, which is beyond the limitation of the intrinsic bandgap of Si and CdS. Fig. 9a demonstrates the schematic structure of the p-Si/n-CdS heterostructure photodetector. The silicon wafer substrate is first etched with KOH to make it flexible (Fig. 9b1). Tetrahedral-shaped microstructures are then etched onto the surface of the flexible wafer to enhance the light absorption efficiency (Fig. 9-b2-4). The on–off current responses at zero bias voltage under different wavelengths are illustrated in Fig. 9c. The p-Si/n-CdS heterostructure photodetector shows a good photoresponse from the UV to NIR wavelengths. The photocurrent of the device is in the microampere range at 325, 442, and 1060 nm wavelengths. However, under 1550 nm laser irradiation, the photocurrent is only in the nanoampere range due to the lack of photogenerated

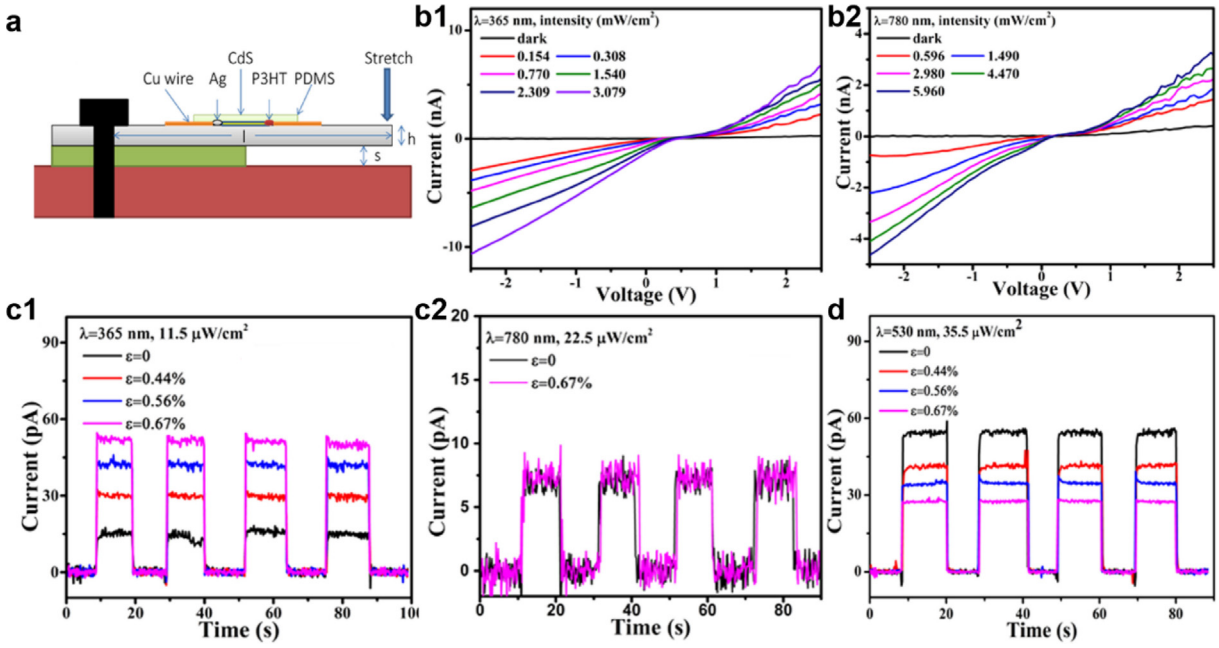

FIG. 8

CdS-P3HT organic/inorganic heterojunction photodetector. (a) Schematic of the measurement setup. *I-V* characteristics with various power densities under (b1) 365 nm and (b2) 780 nm laser illuminations. The effect of positive piezoelectric potential on the photoresponse under (c1) 365 nm, and (c2) 780 nm laser illuminations. (d) The effect of negative piezoelectric potential on the photoresponse under 530 nm laser illumination. Reproduced with permission [100]. Copyright 2017, Elsevier Ltd.

Please cite this article in press as: S. Tian et al., Materials Today, (2023), https://doi.org/10.1016/j.mattod.2023.07.001

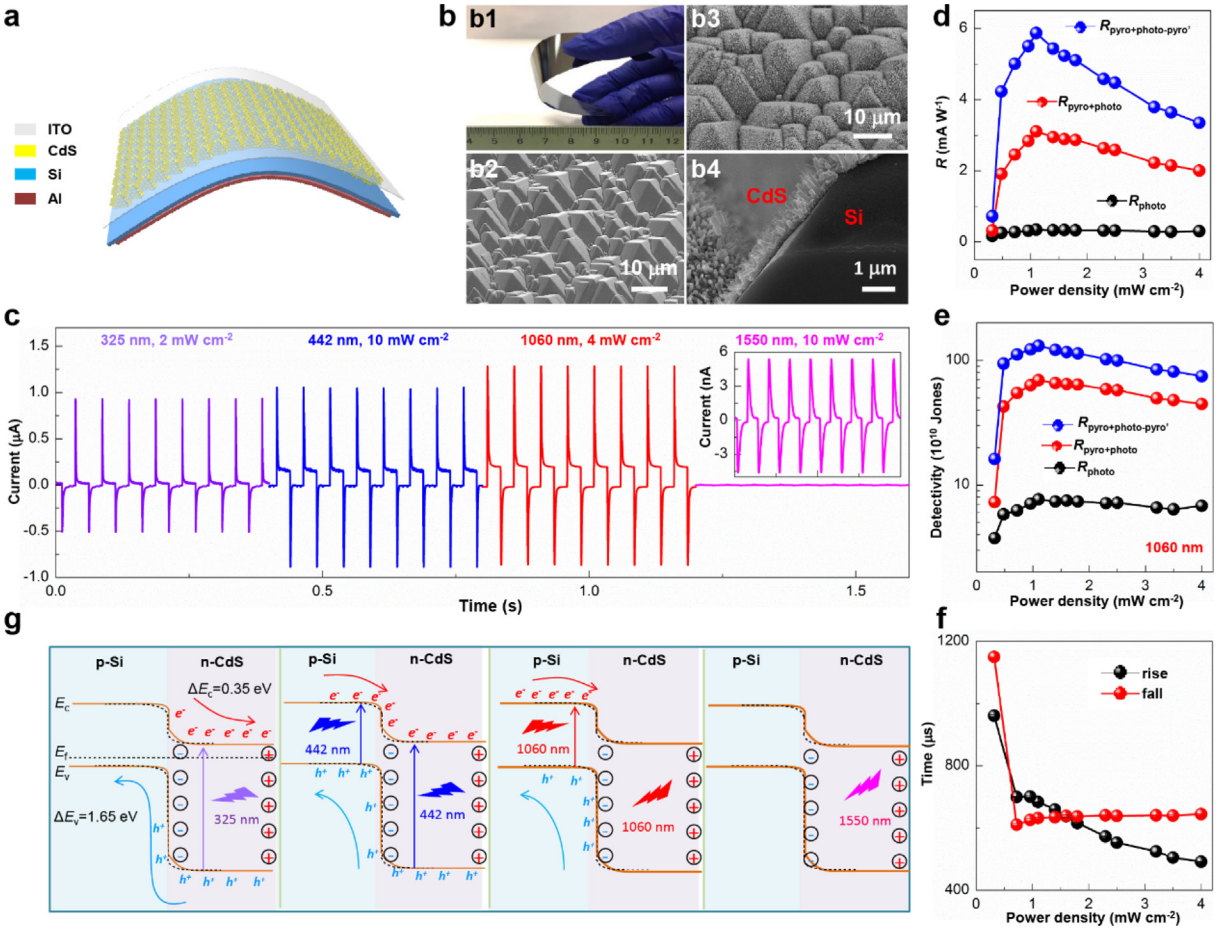

FIG. 9

A p-Si/n-CdS nanowires heterostructure photodetector. (a) Schematic structure of the photodetector. (b) Characterizations of the heterostructure: (b1) flexible Si wafer etched in the KOH solution, (b2) SEM image of the etched Si wafer surface, (b3) top view, and (b4) side view of the CdS NW array. (c) *I-t* curves of the photodetector under 325, 442, 1060, and 1550 nm laser illuminations at zero bias. (d) Photo-responsivity *R* and (e) specific detectivity *D** of photocurrent (I_{photo}), photocurrent + pyroelectric current ($I_{pyro+photo}$), and relative peak-to-peak current ($I_{pyro+photo}$-$I_{pyro'}$) under different power densities at 1060 nm laser illumination. (f) Response time of the photodetector as a function of power density at 1060 nm laser illumination. (g) Schematic band diagrams of the photodetector under different wavelengths of laser illumination. Reproduced with permission [22]. Copyright 2018, Wiley-VCH.

carriers. The photoresponsivity *R* and specific detectivity *D** of photocurrent (I_{photo}), photocurrent + pyroelectric current ($I_{pyro+photo}$), and relative peak-to-peak current ($I_{pyro+photo}$-$I_{pyro'}$) under different power densities are further calculated and plotted in Fig. 9d, e. The photoresponsivity *R* increases with power density due to an increase in photogenerated carrier separation efficiency. The maximum values of R_{photo}, $R_{pyro+photo}$, $R_{pyro+photo-pyro'}$ are 0.34, 3.1, and 5.9 mA W_{-1} under 1060 nm laser illumination, respectively. The maximum detectivity *D** reaches 1.3×10^{12} and 6.9×10^{11} Jones according to the $I_{pyro+photo}$-$I_{pyro'}$ and $I_{pyro+photo}$. Moreover, a fast response time is obtained for the self-powered photodetector (Fig. 9f). As the power density increases, the response becomes faster, which can be explained by the fact that the pyroelectric current is determined by the rate of change in temperature (d*T*/d*t*). The greater the incident power density, the faster the temperature change rate, inducing a larger I_{pyro} and shorter response times. The photodetector has a fast response speed, and the rise time and fall time are 245 μs and 277 μs under 325 nm laser illumination, respectively, which are faster than most reported CdS detectors [22]. To illustrate the mechanism of the broadband photoresponse of the p-Si/n-CdS heterostructure, the energy band diagrams under different wavelength illuminations are shown in Fig. 9g. For UV light at 325 nm, the photons are mainly absorbed by CdS NWs, leading to a photocurrent, and the upward bending of the energy band and pyroelectric potential facilitates the transport of carriers. For visible light at 442 nm, the photons are absorbed by both p-Si and CdS NWs, resulting in a larger photocurrent, which also indicates that the photocurrent is mainly generated by the photogenerated carriers of the Si substrate. Since photons in the NIR can also be absorbed by p-Si, the photocurrent intensity continues to increase under 1060 nm laser illumination. For 1550 nm laser illumination, since this wavelength is beyond the bandgap limitation of the p-Si and CdS NWs, photogenerated carriers could not be produced. However, the pyroelectric effect could still lead to the formation of pyrocharges, form the E_{pyro}, and thus induce an instantaneous rise or drop in the output current with a low value of current.

Please cite this article in press as: S. Tian et al., Materials Today, (2023), https://doi.org/10.1016/j.mattod.2023.07.001

Tri-layers structure

Numerous studies have demonstrated the application of the pyro-phototronic effect to enhance the broadband photoresponse of photodetectors [33,105,106]. In addition, an introduction of an insulating layer in the middle of the p-n junction will facilitate the separation and collection of carriers [91]. A ZnO/NiO/Si heterojunction photodetector is fabricated by introducing a NiO layer between the p-Si and n-ZnO, and thus the leakage current is decreased to improve the pyro-phototronic effect. Moreover, selective response to UV or visible light is achieved by taking advantage of the different current characteristics modulated by bias voltage [107]. Fig. 10a is a schematic representation of the structure of a ZnO/NiO/Si heterojunction photodetector. A Ni layer is first deposited on a Si substrate, and then Ni is oxidized to NiO by thermal oxidation, followed by the growth of ZnO nanorods on the NiO layer by a simple hydrothermal reaction, using Al and Cu as the top and bottom electrodes, respectively. The *I-V* curves of the ZnO/NiO/Si heterojunction photodetector in the dark and under 367, 448, and 609 nm illuminations are demonstrated in Fig. 10b. Both UV and visible light illuminations produce excellent photoresponses. The photocurrent responses of the photodetector under 367 and 609 nm illuminations at forward, zero, and negative bias voltages are shown in Fig. 10c, which exhibit the typical four-stage photocurrent response behavior. Fig. 10d demonstrates the selective photoresponse of the ZnO/NiO/Si heterojunction photodetector under 367, 448, and 609 nm illuminations. Interestingly, at a small forward bias, the ZnO/NiO/Si heterojunction photodetector displays different responses to UV and visible light. When under visible continuous illumination, the local electric field intensity is not sufficient to separate the electron-hole pairs, resulting in little change in the current. However, under continuous UV illumination, the photocurrent gradually increases due to the photoconduction effect of ZnO nanorods, indicating the broadband photoresponse characteristic and wavelength selectivity for UV and visible light.

ZnO/CuO/Au heterojunction photodetector coupled with the localized surface plasmon resonance (LSPR)

To further improve the performance of photodetectors or gain more functionality, lots of studies have been conducted to combine the pyro-phototronic effect with other physical effects to achieve synergistic action [108–111]. The pyroelectric current relies on the temperature variation, but the weak temperature variation at low power density illumination makes it difficult to detect this kind of photons for the pyro-phototronic effect modulated photodetectors [112]. However, the localized surface plasmon resonance (LSPR) can produce instantaneous and rapid temperature change, which is beneficial for the pyro-phototronics based photodetectors [113–116]. LSPR is the phenomenon of local surface plasmon resonance, accompanied by a rapid rise in temperature, that occurs when light is incident on nanoparticles made of precious metals and if the frequency of the incident photons matches the overall vibrational frequency of the conduction electrons of the precious metal nanoparticles or metal, the nanoparticles or metal will have a strong absorption of the photon energy [117]. The response speed of a ZnO/CuO/Au heterojunction photodetector has been greatly improved due to the rapid temperature change by coupling the pyro-phototronic effect with the LSPR [118]. Fig. 11a

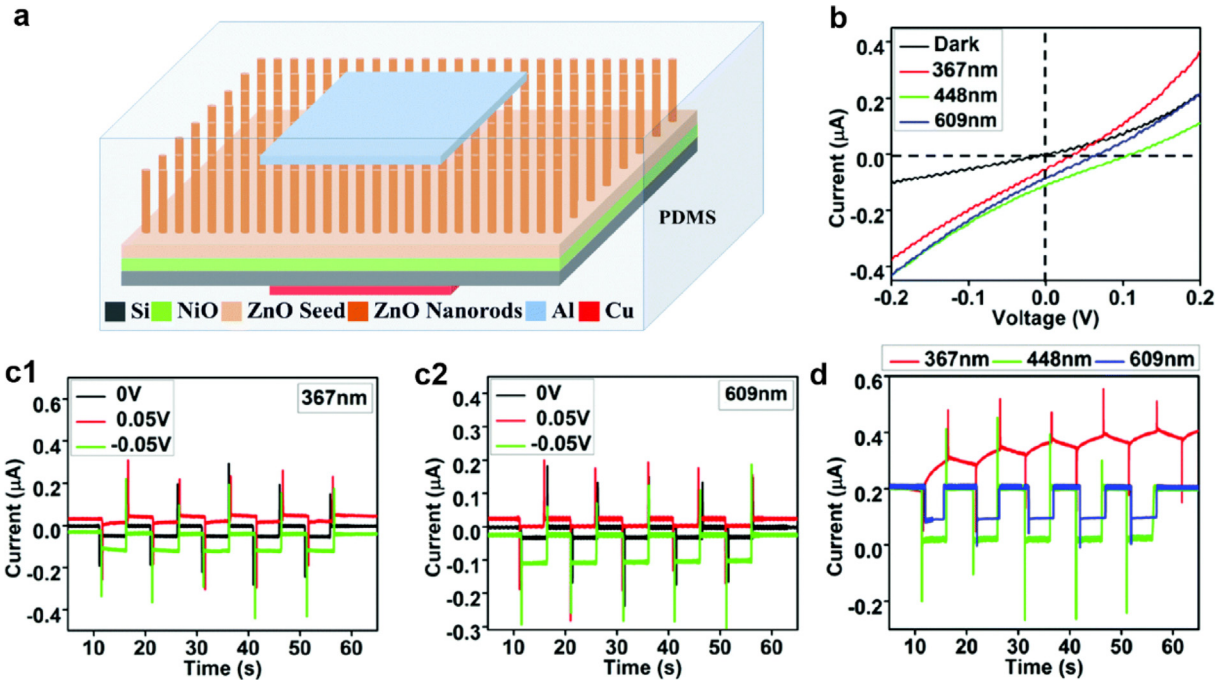

FIG. 10

A ZnO/NiO/Si heterojunction photodetector. (a) Schematic representation of the structure of the photodetector. (b) *I-V* characteristic of the ZnO/NiO/Si heterojunction photodetector in the dark and under 367 nm, 448 nm, and 609 nm illuminations. Photocurrent responses of the photodetector under (c1) 367 nm, and (c2) 609 nm illuminations at forward, zero, and negative bias. (d) Photoresponse of the photodetector under 367 nm, 448 nm, and 609 nm illuminations at 0.001 V bias voltage. Reproduced with permission [107]. Copyright 2017, Royal Society of Chemistry.

Please cite this article in press as: S. Tian et al., Materials Today, (2023), https://doi.org/10.1016/j.mattod.2023.07.001

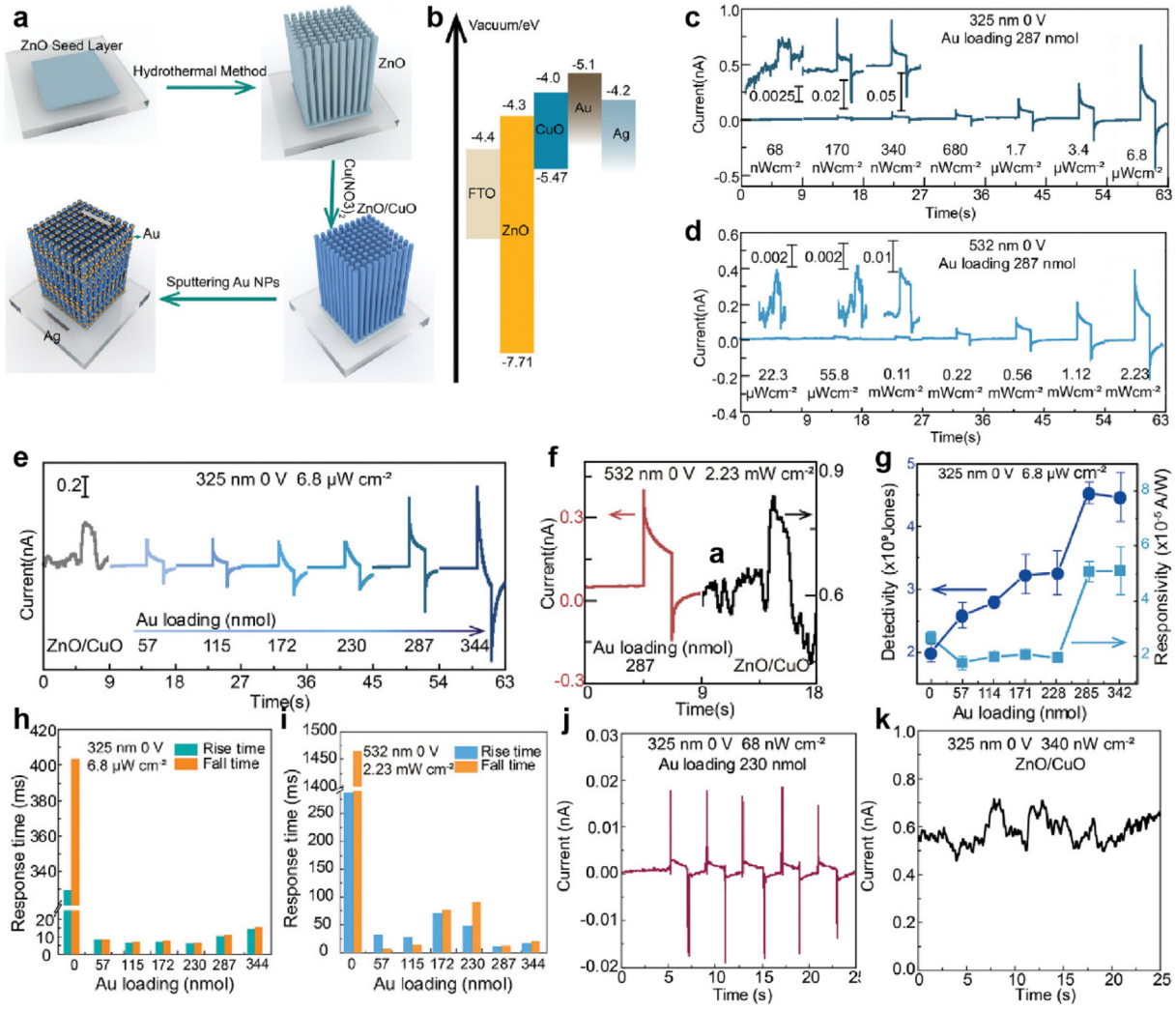

FIG. 11

A ZnO/CuO/Au heterojunction photodetector. (a) The flow chart for the fabrication of the ZnO/CuO/Au heterojunction photodetector. (b) Energy band diagram of the ZnO/CuO/Au heterojunction. *I-t* curves of the photodetector under (c) 325 nm and (d) 532 nm illuminations with various power densities. (e) *I-t* characteristics of the photodetector with different Au loadings. (f) *I-t* characteristics of the photodetector with or without the Au NPs. (g) Responsivity and detectivity of the photodetector with various Au loadings. Response times of the photodetectors under (h) 325 nm illumination and (i) 532 nm illumination. Photoresponse behavior (j) with and (k) without Au NPs under 325 nm laser illumination. Reproduced with permission [118]. Copyright 2022, Wiley-VCH.

is a flow chart of the fabrication of this ZnO/CuO/Au heterojunction photodetector. The ZnO nanorods are hydrothermally grown on the ZnO seed layer before being coated with a CuO layer in a $Cu(NO_3)$ solution. Finally, Au nanoparticles (NPs) are decorated on the nanorods to provide the LSPR effect. Ag and FTO are the top and bottom electrodes, respectively. The vacuum energy level of materials indicates that the photodetector has a good energy band match (Fig. 11b). The *I-t* curves of photodetectors under 325 and 532 nm illuminations from 68 nW cm^{-2} to 6.8 μW cm^{-2} are plotted in Fig. 11c, d. The photocurrent increases with increasing power density due to the increase in photogenerated electron-hole pairs. Meanwhile, all the curves exhibit typical four-stage photoresponse dynamic behavior due to the pyro-phototronic effect. Compared with the ZnO/CuO heterojunction, the photodetector with the Au loading has a better signal-to-noise ratio. Besides, the photocurrent gradually increases with the loading of Au NPs (Fig. 11e). The same results are also obtained at 532 nm illumination (Fig. 11f). The responsivity R and detectivity D^* of the ZnO/CuO/Au heterojunction photodetector are also investigated. As shown in Fig. 11g, the maximum of R and D^* are 5.07×10^{-5} A W^{-1} and 4.53×10^{9} Jones under the illumination of a 325 nm laser at the loading of 287 nmol, respectively. In addition, attributed to the fast temperature variation induced by the LSPR effect, the response time is dramatically reduced. For 325 nm laser illumination, the rise and fall times are decreased from 329.6 ms to 6.3 ms, and 403.7 ms to 6.9 ms (Fig. 11h). For 532 nm laser illumination, the response time has also been significantly reduced (Fig. 11i). Furthermore, to demonstrate the ability of the ZnO/CuO/Au heterojunction photodetector to detect ultralow power density laser, the photoresponse with and without Au NPs under 325 nm laser illumination are shown in Fig. 11j, k, respectively. The ZnO/CuO/Au heterojunction photodetector exhibits an excellent photoresponse under a power density of 68 nW cm^{-2}, but the ZnO/CuO photodetector cannot obtain a regular photocurrent curve even under a 360 nW cm^{-2} power density.

Please cite this article in press as: S. Tian et al., Materials Today, (2023), https://doi.org/10.1016/j.mattod.2023.07.001

$BiFeO_3$/Au/ZnO heterostructure photodetector coupled with the ferroelectricity and LSPR

Materials used in the pyro-phototronic effect are often accompanied by piezoelectric and ferroelectric properties [13,119], and thus coupling the pyro-phototronic effect with the ferroelectric effect is a common approach [120,121]. $BiFeO_3$ (BFO) is a typical ferroelectric material with a small band gap (2.2–2.8 eV) and excellent light absorption [122,123], and the large coercive field of BFO facilitates the separation of photogenerated carriers [124,125]. However, ferroelectric-semiconductor heterojunctions usually absorb high-frequency light well, but the absorption of NIR light is negligible [126–128]. The LSPR effect achieved by introducing noble metal nanoparticles into the ferroelectric layer is found to be effective in broadening the spectral response range [129,130]. A $BiFeO_3$/Au/ZnO heterostructure photodetector is fabricated [131]. With the help of the modulation of the Schottky barrier and the band alignment at the heterostructure interface by Au NPs, the response range is successfully broadened from 360 nm to 1060 nm light wavelengths, which is beyond the bandgap limitation.

Fig. 12a shows the XRD pattern of the BFO, indicating the successful fabrication of the BFO. The interface of the heterojunction can be seen clearly in the scanning electron microscope (SEM) image in Fig. 12b. A comparison of the light absorption of different materials in the UV–Vis spectrum is shown in Fig. 12c. The BFO/Au/ZnO shows the strongest absorption intensity accompanied by a broadband response. Fig. 12d shows the variation of current density at zero bias voltage for the BFO/Au/ZnO heterostructure under different illumination wavelengths, indicating large photocurrent density in the UV–Vis-NIR band, which is beyond the bandgap limitation. Fig. 12e shows the *J-T* curves of the BFO/Au/ZnO device under the 360, 405, 532, and 635 nm illuminations at zero bias voltage. All curves exhibit a two-step waveform, that is, a sharp current peak followed by a flat plateau. The sharp current peaks are caused by the pyro-phototronic effect, while the plateau is caused by the photovoltaic effect.

The energy band diagram in Fig. 12f illustrates the mechanism for the enhanced photosensing of the BFO/Au/ZnO heterostructure. When Au nano-particles (AuNPs) are introduced, two interfaces, BFO/Au and Au/ZnO, are formed in the contact region. The Schottky contact and energy band bending are formed at the BFO/Au interface (Fig. 12f1). Since AuNPs can facilitate the transfer of hot electrons through the LSPR effect, the BFO/Au interface has a similar interface characteristic to the Au/ZnO interface. The built-in electric field at the Au/ZnO interface and the depolarization field (E_{dp}) of BFO become the main factors influencing the separation of photogenerated carriers. When illuminated with 360 nm and 405 nm lasers (Fig. 12f2, f3), the temperature of the illuminated area rises, and negative pyroelectric charges are generated at the Au/ZnO interface, which will repel the electrons away from the interface and bend the energy band upward. In addition, the rise in temperature decreases the E_{dp} of the BFO, again promoting the upward bending of the energy band. These promote the separation of photogenerated carriers, which leads to instantaneous pyroelectric currents (sharp current peaks in the first step). As the wavelength of the laser continues to increase until it is beyond the absorption band range of the BFO and ZnO, the hot electrons can gain enough energy to transfer from AuNPs to the two Schottky contact interfaces, and the energy band at the interface still can bend upwards (Fig. 12f4). With the help of the LSPR effect, the self-polarization of BFO films, and the band bending of the heterostructures, the BFO/Au/ZnO heterostructure photodetector successfully achieves the broadband photoresponse from 360 nm to 1060 nm.

Anodic aluminum oxide/CdS heterostructure photodetector coupled with photothermoelectric effect

CdS is widely used not only in the pyro-phototronic effect-enhanced photodetectors, but it also has a thermoelectric effect [132]. Coupling the photo-pyroelectric effect and photo-thermoelectric effect can further enhance the photoresponse of the CdS-based photodetector [133]. A polar bear-inspired (PBI) PD based anodic aluminum oxide (AAO) and CdS with an asymmetric pair of Ag (PBI_AAO/CdS_asy-Ag PD) is fabricated to achieve broadband photosensing by the synergy between the pyroelectric effect and the thermoelectric effect [134]. Fig. 13a shows the fabrication procedure for this PBI_AAO/CdS_asy-Ag photodetector. The PBI_AAO is first anodized on the aluminum foil to reduce the light reflection and enhance the absorption. The CdS NWs are then grown on the previous structure using a hydrothermal method. Finally, a pair of asymmetric Ag electrodes are coated on both ends of the device.

Fig. 13b shows the *I-t* on–off test of the PBI_AAO/CdS_asy-Ag photodetector under different wavelengths of laser illumination, which exhibits the typical four-stage photoresponse dynamic behavior. For 405 nm spectrum illumination, due to the weak photo-thermoelectric effect, the steady current plateau is mainly caused by the photovoltaic effect (Fig. 13b1). However, when the wavelength increases to 532 nm (Fig. 13b2), an obvious four-stage photoresponse behavior appears. In the first stage, a sharp peak of current is induced by the instantaneous temperature change, which is contributed by the pyro-phototronic effect and the photogenerated carriers produced by the CdS. In the meantime, a spatial temperature gradient formed between the asymmetric Ag electrode pair. Therefore, the current is caused by the photovoltaic effect, the photo-pyroelectric effect, and the photo-thermoelectric effect. When the temperature is stable, the pyroelectric effect disappears, and a stable current plateau is contributed by the thermoelectric effect and photovoltaic effect (the second stage). In the third stage, the laser is turned off, resulting in a decreased temperature, a reversed pyroelectric potential, and a temperature gradient between the asymmetric electrodes. Therefore, the pyroelectric current is the opposite of the thermoelectric and photovoltaic currents (the third stage). When the wavelength of the spectrum reaches 660 nm and 808 nm (Fig. 13b3, b4), since the wavelengths are beyond the bandgap of CdS, the photogenerated carriers disappear. In the first stage, only pyroelectric and thermoelectric currents exist. When the temperature is constant in the second stage, the pyroelectric current disappears, resulting in a decreased peak current. The steady current is formed by the thermoelectric effect caused by the asymmetric Ag electrode pair. With the laser off, the decreasing temperature causes a reversed pyroelectric current. The reversed direction of the pyroelectric current and thermoelectric current makes the current in the third stage less than

Please cite this article in press as: S. Tian et al., Materials Today, (2023), https://doi.org/10.1016/j.mattod.2023.07.001

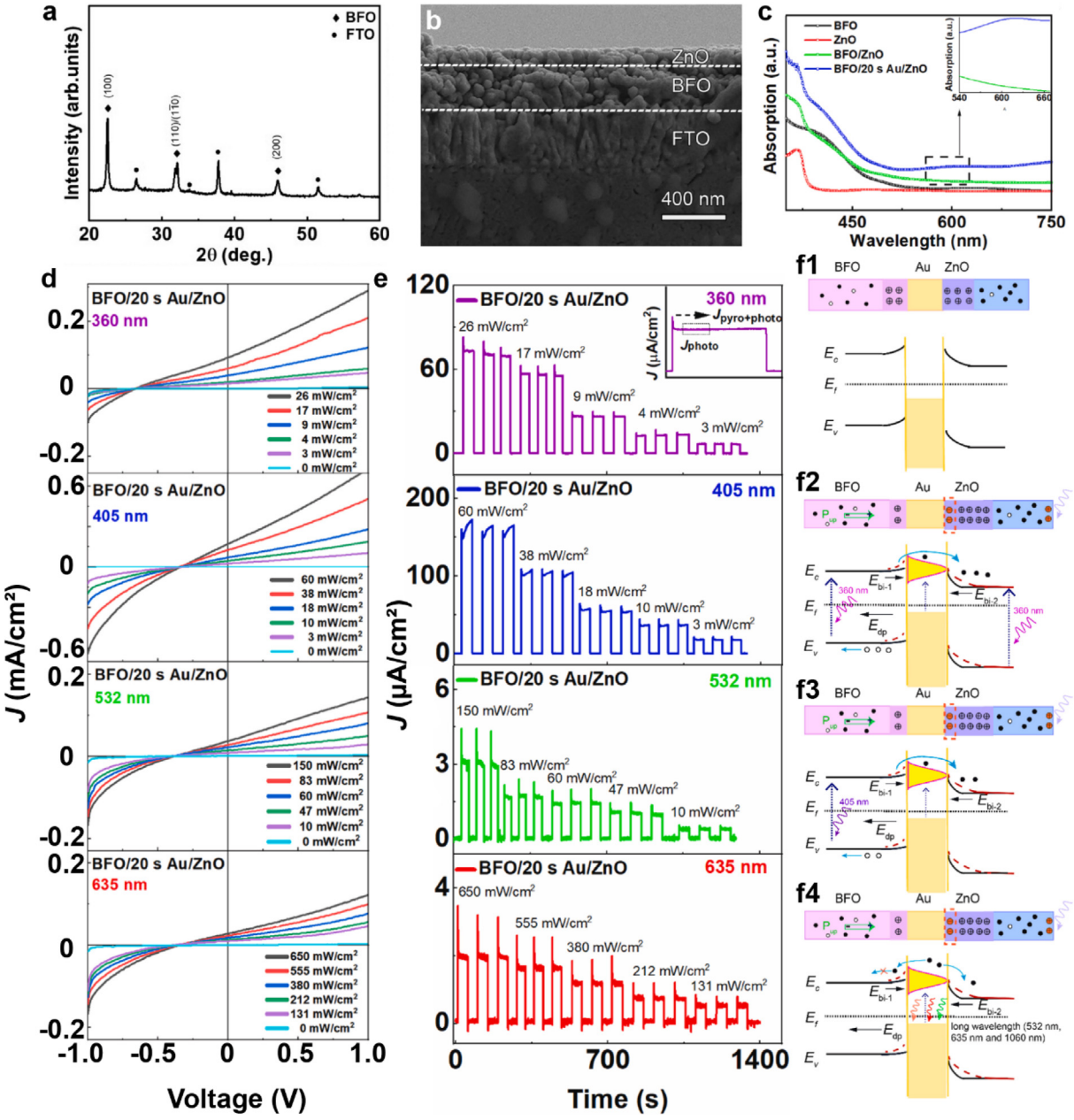

FIG. 12

A $BiFeO_3$/Au/ZnO heterostructure photodetector. (a) XRD patterns of BFO films. (b) A cross-section SEM image of BFO/ZnO heterostructures. (c) Absorption spectra of BFO, ZnO, BFO/ZnO and BFO/20 s Au/ZnO. (d) Variation of current density of BFO/ Au/ZnO heterostructures under 360 nm, 405 nm, 532 nm, and 635 nm light illuminations with different power densities. (e) *J-T* curves at zero bias for the BFO/Au/ZnO heterostructure under 360 nm, 405 nm, 532 nm, and 635 nm light illuminations. (f) Schematic energy band diagrams of the BFO/Au/ZnO heterostructure under different wavelength illuminations. Reproduced with permission [131]. Copyright 2021, Elsevier Ltd.

the first stage. As shown in Fig. 13c-f, under laser illumination, the asymmetric Ag electrode pair causes the difference in shading light, and the photodetector is warmed with a temperature gradient between the asymmetric electrode pair, showing d*T*/d*x* greater than 0 along the direction from the small Ag electrode (warm side) to the large Ag electrode (cool side).

Ag_2Se/Si heterostructure photodetector coupled with the lateral photovoltaic effect (LPE)

Ag_2Se is a typical thermoelectric material [135–137], which has rarely been applied in the photoelectric field [138–140], especially in position-sensitive detectors (PSDs). Since the photovoltage is linear to the laser distance, the PSD based on the LPE effect is suitable for ultra-high accuracy displacement sensing [141,142]. A self-powered Ag_2Se/Si heterostructure PSD based on the LPE is fabricated, with the merits of broadband and ultrafast photoresponse [143]. Fig. 14a shows the structural schematic of the heterostructure. A layer of Ag_2Se films is sputtered on p-Si substrates using magnetron sputtering, and two indium pads are coated on the film to act as the electrode. The photoabsorption spectra of the Ag_2Se films with different thicknesses are shown in Fig. 14b. For all the films with different thicknesses, a broad

Please cite this article in press as: S. Tian et al., Materials Today, (2023), https://doi.org/10.1016/j.mattod.2023.07.001

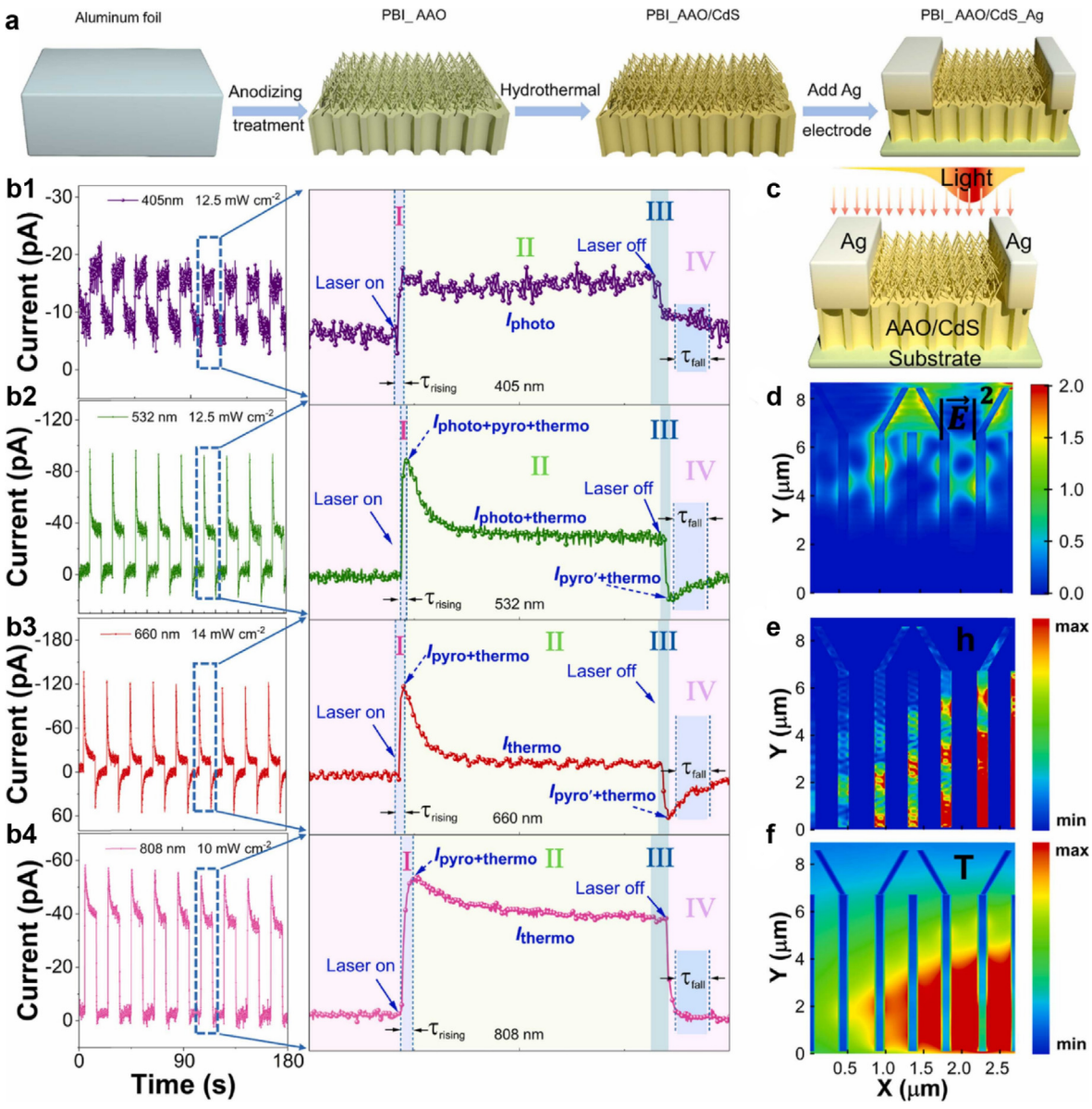

FIG. 13

A PBI_AAO/CdS_asy-Ag photodetector. (a) Fabrication process of the photodetector. *I-t* on–off test of the photodetector under (b1) 405 nm, (b2) 532 nm, (b3) 660 nm, and (b4) 808 nm light illuminations. (c) Schematic measurement of the photodetector: (d) simulated $|\vec{E}|^2$ profile, (e) heat source profile, and (f) temperature profile of the photodetector at the wavelength of 660 nm. Reproduced with permission [134]. Copyright 2022, Elsevier Ltd.

absorption range from 300 to 1200 nm is obtained, which indicates that the heterostructure PSD has broadband response characteristics. Fig. 14c shows the lateral photovoltage (LPV) curves under different laser wavelengths. The LPV increases with the wavelengths from 405 to 1064 nm, but has no response under 1150 nm laser illumination, which can be explained by the band gap of the Ag_2Se. Although bulk Ag_2Se is often accompanied by a narrow band gap (0.15 eV), it is generally between 1.1 and 2.1 eV for thin film materials. The LPV curves show a linear dependence on the laser position for different wavelengths, revealing its application in the fields of broadband photosensing and position-sensitive detection. The sensitivity of the heterostructure is calculated and plotted in Fig. 14d. With the increment in wavelength, the sensitivity of the heterojunction is also enhanced with increasing laser power. The *I-t* curves of the heterojunction under different wavelengths of laser illumination are shown in Fig. 14e. All the curves exhibit the typical four-stage LPV dynamic behavior induced by the pyro-phototronic effect, which indicates the ability of a broadband response modulated by the pyro-phototronic effect. The LPV_{py+ph}-$LPV_{py'}$, LPV_{py+ph}, LPV_{ph}, and corresponding enhancement ratios of (LPV_{py+ph}-$LPV_{py'}$)/LPV_{ph} and LPV_{py+ph}/LPV_{ph} are calculated and plotted in Fig. 14f, g. All the LPV responses exhibit a monotonic incremental tendency with the increment of wavelength. The maximal enhancement ratios are 1643% and 1057%, respectively, obtained at 1064 nm laser wavelength. Moreover, the response time under different chopper frequencies is systematically investigated (Fig. 14h). With a frequency increasing from 10 to

Please cite this article in press as: S. Tian et al., Materials Today, (2023), https://doi.org/10.1016/j.mattod.2023.07.001

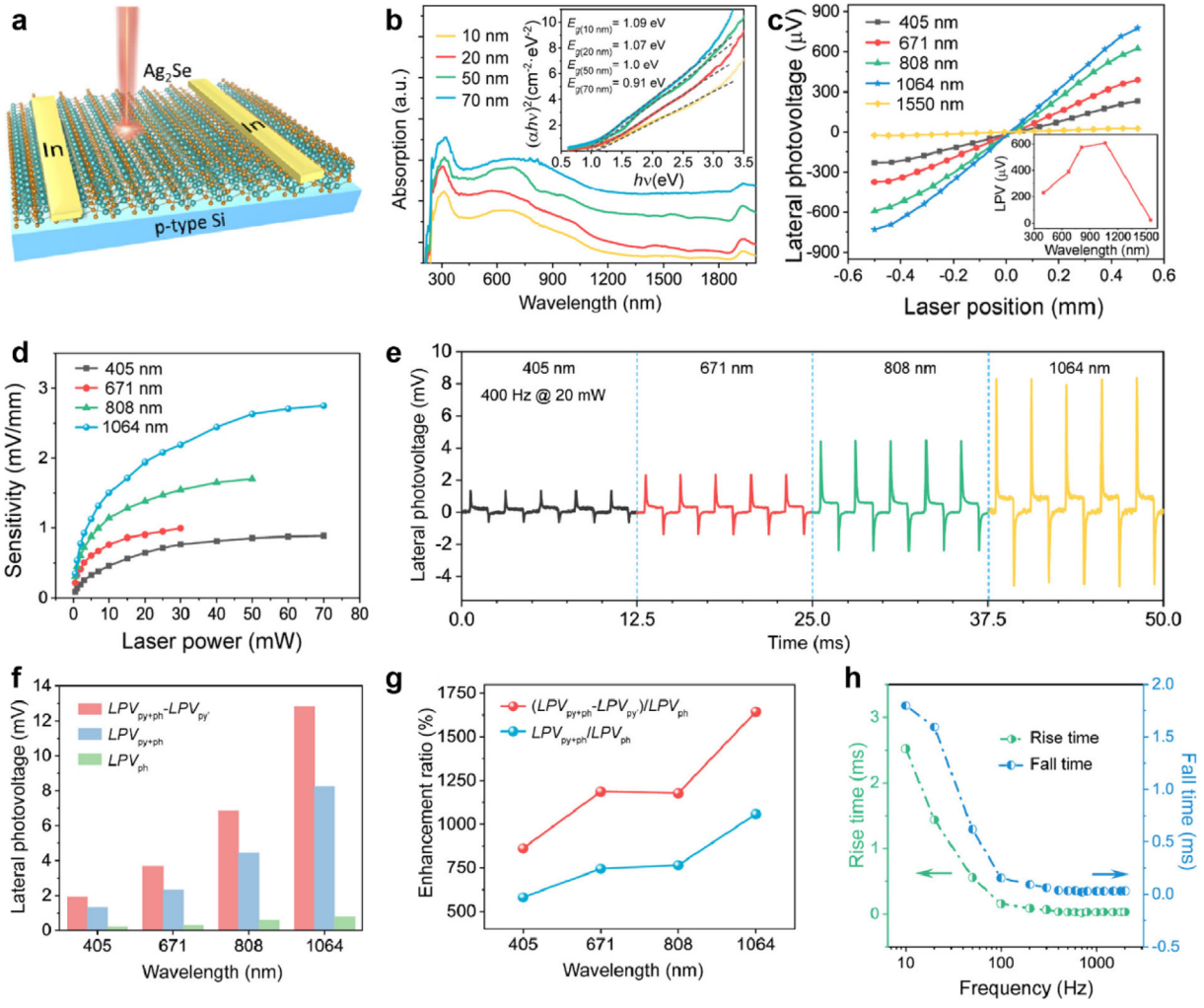

FIG. 14

A self-powered Ag_2Se/Si heterostructure. (a) Structural schematic of the heterostructure. (b) Photoabsorption spectra of the Ag_2Se films with different thicknesses. (c) Lateral photovoltage curves under different laser wavelength illuminations, with the inset showing the calculated $(\alpha h\nu)^2$ vs photon energy ($h\nu$) characteristics. (d) Sensitivity of the LPV at different wavelengths with various laser powers. (e) *I-t* curves of the heterojunction under different wavelengths of laser illumination. (f) $LPV_{py+ph} - LPV_{py'}$, LPV_{py+ph}, LPV_{ph}, and (g) corresponding enhancement ratios of $(LPV_{py+ph} - LPV_{py'})/LPV_{ph}$ and LPV_{py+ph}/LPV_{ph} as a function of the laser wavelength. (h) Response time as a function of the chopper frequency. Reproduced with permission [143]. Copyright 2022, American Chemical Society.

2000 Hz, the rise time decreases from 2.5 ms to 3 μs, and the fall time decreases from 1.8 ms to 5 μs, which demonstrates an ultrafast response characteristic.

Broadband photodetectors based on the synergy of the piezo/pyro-phototronic effect

The piezo-phototronic and pyro-phototronic effects have demonstrated the great potential for enhanced performance of broadband photosensing. These works illustrated above are modulated by the piezo-phototronic effect or the pyro-phototronic effect individually on the photodetectors. However, some materials usually possess both piezoelectric and pyroelectric effects [144,145], so it is possible to enhance the performance of a photodetector through the synergistic effect of the piezo-phototronic and pyro-phototronic effects [13,146–148]. The piezo-phototronic effect derived from piezo/pyroelectric semiconductors can be introduced and modify the photoresponse performance of the heterojunction photodetectors when under deformation. If the piezocharges produced by external strain and the pyrocharges produced by the changed temperature are both negative (or both positive) at the interface, the strain would strengthen the pyroelectric potential and thus enhance the pyro-phototronic effect-induced photocurrent; otherwise, it would weaken the photocurrent. The piezocharges, work together with the pyrocharges, can facilitate carrier separation and collection, thus enhancing photocurrent [13,22]. Yang *et al*. successfully fabricate a $MAPbI_3$ single-crystal film/n-Si heterojunction photodetector, which enhances the performance of the broadband photodetector through the synergistic effect [149].

Fig. 15a shows the structural schematic of the photodetector. The $MAPbI_3$ single crystal films are grown on the n-Si substrate directly through a space-confined slow heating method. The top and bottom electrodes are ITO and Al, respectively.

Please cite this article in press as: S. Tian et al., Materials Today, (2023), https://doi.org/10.1016/j.mattod.2023.07.001

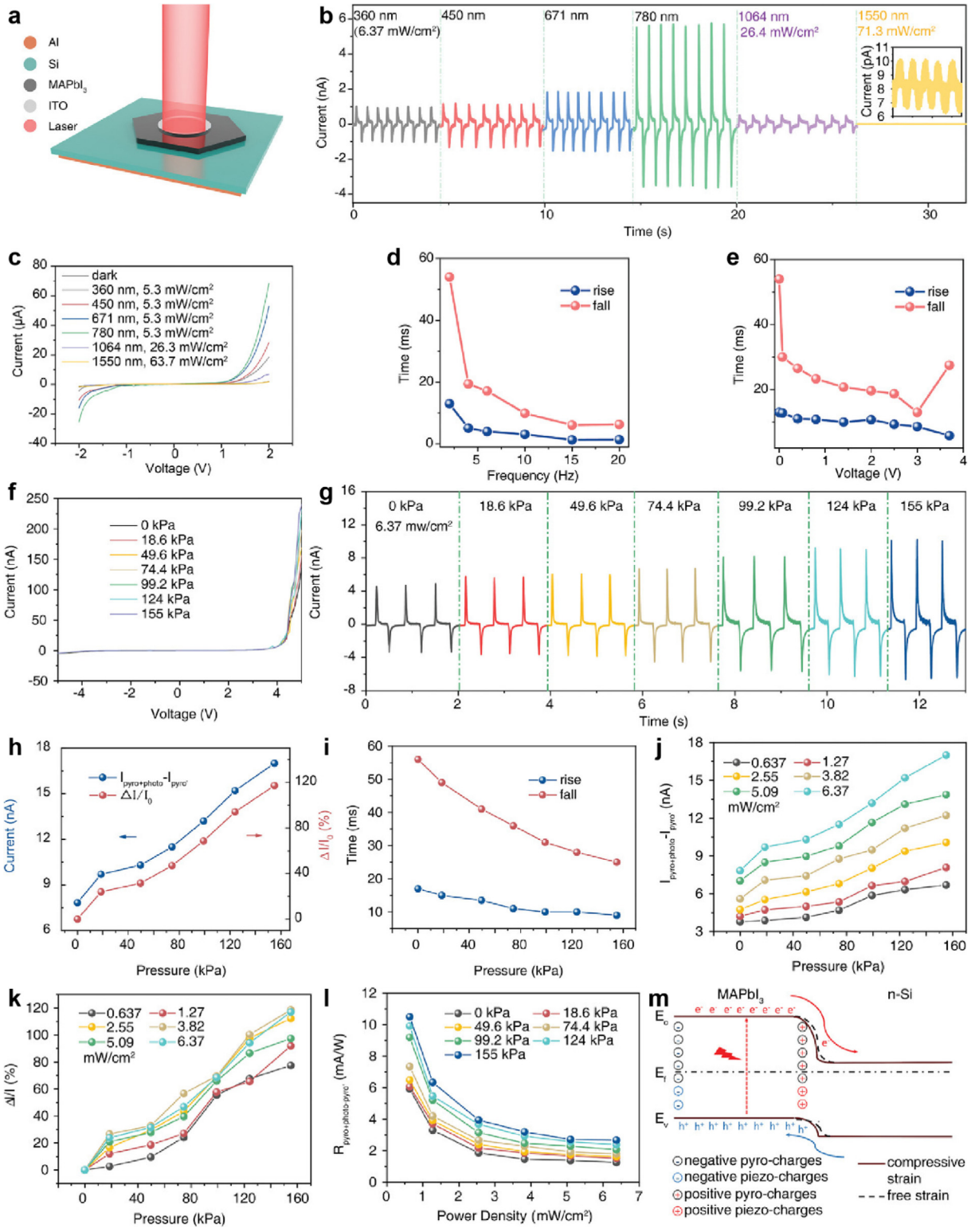

FIG. 15

A $MAPbI_3$ single-crystal film/n-Si heterojunction photodetector. (a) Structural schematic of the heterojunction photodetector. (b) Photoresponse of the photodetector under 360, 450, 671, 780, 1064, and 1550 nm laser illuminations at zero bias. (c) *I-V* curves of the photodetector under different laser illuminations. Response time for different (d) chopper frequencies and (e) voltages. (f) Comparison of the photoresponse under the pressure from 0 to 155 kPa in the dark condition. (g) On-off current response at zero bias of the photodetector for 780 nm laser illumination under different pressures. (h) Peak current, relative change of $\Delta I/I_0$, and (i) response time under different pressures at 780 nm laser illumination of 6.37 mW cm^{-2}. (j) $I_{pyro+photo}$-$I_{pyro'}$ and (k) relative change of $I_{pyro+photo}$-$I_{pyro'}$ as a function of pressure under different power densities. (l) Responsivities $R_{pyro+photo-pyro'}$ as a function of power density under different pressures. (m) Energy band diagrams of the photodetector with or without a compressive strain. Reproduced with permission [149]. Copyright 2021, Wiley-VCH.

Please cite this article in press as: S. Tian et al., Materials Today, (2023), https://doi.org/10.1016/j.mattod.2023.07.001

Fig. 15b shows the photoresponse of the photodetector under 360, 450, 671, 780, 1064, and 1550 nm laser illuminations at zero bias voltage, which exhibits a typical four-stage photoresponse dynamic behavior for all wavelengths, indicating the existence of the pyro-phototronic effect. The *I-V* curves of the photodetector under different laser illuminations are shown in Fig. 15c. The photocurrent of the photodetector under 780 nm illumination is much larger than other wavelengths. For 1064 nm, the NIR photons can pass through the $MAPbI_3$ single crystal films and can be absorbed by the Si substrate. For 1550 nm, the wide bandgap of $MAPbI_3$ will limit the production of photo-generated carriers. The response time for different chopper frequencies and voltage are plotted in Fig. 15d, e. With the increase in frequency, the rise time is reduced from 13 ms to 1.4 ms, and the fall time is reduced from 54 ms to 6.3 ms, which is attributed to the faster temperature change under higher frequency. With the increase in bias voltage, the rise time is reduced from 12 ms to 4 ms, and the fall time is reduced from 54 ms to 13 ms.

The piezo-phototronic effect is utilized to further enhance the performance of the photoresponse. Fig. 15f is the comparison of the photoresponse under the pressure from 0 to 155 kPa in the dark condition. When pressure is applied, there is a boost in photocurrent at forward bias voltage, indicating the enhancement of photoresponse through the piezo-phototronic effect. The on–off current response at zero bias voltage of the photodetector for 780 nm laser illumination under different pressures is shown in Fig. 15g. Meanwhile, the peak current and the relative change of $\Delta I/I_0$ under different pressure is plotted in Fig. 15h, and the response time is plotted in Fig. 15i. With the increase of pressure from 0 to 155 kPa, the photocurrent increases from 6.75 nA to 16 nA, and the maximum relative current change is 120% obtained at 155 kPa. Besides, the rise time is reduced from 17 ms to 9 ms, and the fall time is reduced from 56 ms to 25 ms. Finally, the $I_{pyro+photo}$ - $I_{pyro'}$, and the relative change of $I_{pyro+photo}$-$I_{pyro'}$, as a function of pressure under different power densities are systematically investigated and plotted in Fig. 15j, k. For all the power densities, the $I_{pyro+photo}$-$I_{pyro'}$ and $\Delta I/I_0$ increase with the increasing pressure, which indicates the enhancement by the introduction of the piezo-phototronic effect. The responsivity $R_{pyro+photo-pyro'}$ decreases with the increasing power density under different pressures (Fig. 15l). The energy band diagram of the heterostructure is utilized to demonstrate the synergistic effect of the piezo-phototronic and pyro-phototronic effects (Fig. 15m). The thickness of the film will decrease with the applied pressure, which introduces the positive piezoelectric charges at the interface to work together with the positive pyroelectric charges. Two types of charges bend the energy band further downwards to facilitate the separation and collection of the carriers. Therefore, the enhancement of the photoresponse is attributed to the synergistic effect of the piezo-phototronic and pyro-phototronic effects. With the help of the synergy between the two physical effects, the response spectrum can be broadened to 360–1550 nm, which is a significant enhancement compared to the two effects working separately [150,151].

Summary and outlook

In summary, this review presents some of the most advanced broadband photoresponse devices based on the piezo-phototronic or pyro-phototronic effects (Table 1). The piezoelectric and pyroelectric potential due to the change in strain or temperature have been proven to have a significant effect on the enhancement of the broadband response of photodetectors. The piezo-phototronic effect, the pyro-phototronic effect, and the piezo/pyro-phototronic synergy effect to enhance photoresponse performance are presented, and the broadband photodetectors with various device structures are summarized in detail. By introducing the piezo-phototronic and pyro-phototronic effects, the photoresponse band, response speed, photoresponsivity, and specific detectivity of the optoelectronic devices are greatly improved, and self-powered photosensing can be realized without the need for an external power supply. This review offers a comprehensive understanding of the piezo-phototronic and pyro-phototronic effects, which are anticipated to improve wearable sensors, photothermal detection, ultra-fast optics, optical communications, health monitoring, and other fields.

Despite significant progress in recent years in improving broadband photosensing through the piezo- and pyro-phototronic effects, some challenges and obstacles remain (Fig. 16). Firstly, the current device structures are generally based on one-dimensional materials like nanowires and nanorods, so what about two-dimensional materials? How will it work? Two-dimensional materials, which are currently the focus of research, are more sensitive than one-dimensional materials, and thus introducing the piezo-phototronic and pyro-phototronic effects into two-dimensional piezoelectric materials may bring unexpectedly excellent results. Secondly, in order to bring this technology to market, durability is a key factor. Nanomaterials possess good mechanical durability, but the deposited electrode materials and the substrates tend to fail under repeated strain and temperature stimulation. It is therefore particularly important to improve the flexibility and durability of the electrode and substrate materials, or to develop new materials (for example, conducting polymers). Third, the current structure of the photodetector device is relatively homogeneous, and more structures can be explored in future research to meet the functional requirements. For example, intensity, response speed, responsivity, and detectivity all require further improvement by designing more diverse structures. Last but not least, the piezo-phototronic and pyro-phototronic effects have shown large potential in broadband photosensing, and thus the wavelength response of the photodetector can be further broadened, from far ultraviolet to mid-infrared wavelengths, for more possible applications. Overall, the piezo-phototronic and pyro-phototronic effects are unique in the modulation of the energy band at the interface, making them a significant improvement to the performance of the photodetector, which is incomparable by conventional photodetection techniques. With the controllable modulation of the piezo-phototronic and pyro-phototronic effects, the optoelectronic devices for broadband photosensing will perform much better in the future.

Please cite this article in press as: S. Tian et al., Materials Today, (2023), https://doi.org/10.1016/j.mattod.2023.07.001

TABLE 1

Comparison of the characteristic parameters of piezo-phototronics and pyro-phototronics enhanced photodetectors.

Physical effect	Photodetectors	Wavelength (nm)	Bias (V)	Responsivity	Detectivity	Rise/fall time	Ref.
Piezo-phototronics	Single CdTe NW	325–808	5	587 mA W^{-1} @ 808 nm	–	0.5/0.45 s	[69]
	CdS NR/rGO	530–1450	0	0.58 mA W^{-1} @ 365 nm	7.2 × 10^{11} Jones @ 365 nm	1.3/1.7 ms	[74]
	CdSe/CdTe NW	385–850	2.5	4.33 μA mW^{-1} @ 850 nm	–	–	[90]
	Si/AlO_x/ZnO NW	442–1060	−2	∼ 1 A W^{-1} @ 442 nm	–	260/220 μs	[92]
	ZnO/Al_2O_3/Si	365–1064	−2	13.8 A W^{-1} @ 365 nm	7.2 × 10^{11} Jones @ 633 nm	< 100 μs	[93]
	CdS/P3HT	365–780	0	–	–	0.2 s	[100]
Pyro-phototronics	Si/CdS	325–1550	0	0.34 mA W^{-1} @ 1060 nm	6.9 × 10^{11} Jones @ 1060 nm	245/277 μs	[22]
	ZnO/NiO/Si	367–609	0	–	–	–	[107]
	ZnO/CuO/Au	325–532	0	0.14 mA W^{-1} @ 325 nm	3.3 × 10^{11} Jones @ 325 nm	∼ 10 ms	[118]
	$BiFeO_3$/Au/ZnO	360–1060	0	–	–	–	[131]
	Ag_2Se/Si	405–1064	0	–	–	3/5 μs	[143]
Synergy effect	$MAPbI_3$/Si	360–1550	0	1.5 mA W-1 @ 780 nm	3.4 × 10^7 Jones @ 780 nm	12/54 ms	[149]

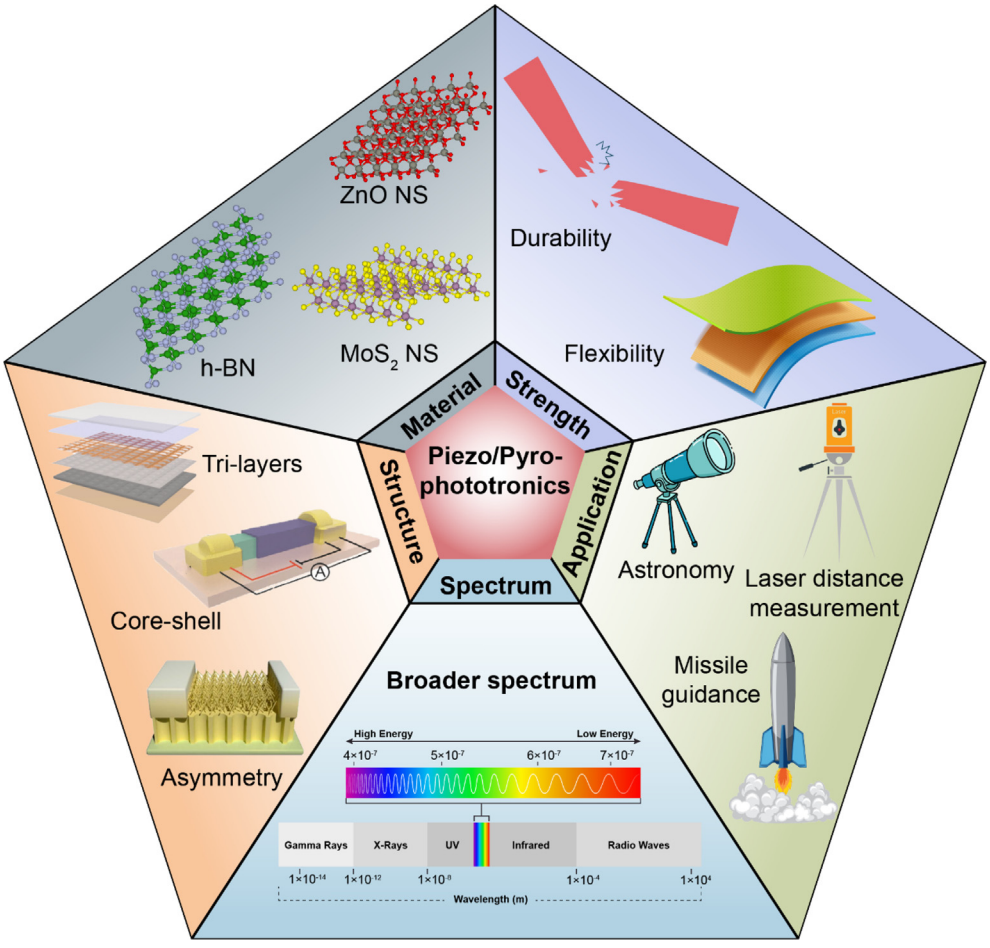

FIG. 16

Summarized future prospects of the piezo-phototronic and pyro-phototronic effects for broadband photosensing.

Data availability

Data will be made available on request.

Declaration of Competing Interest

The authors declare that they have no known competing financial interests or personal relationships that could have appeared to influence the work reported in this paper.

Acknowledgements

This work was supported by the National Key R&D Program of China (Grant No. 2021YFA0716500), the Young Top Talent Project of the National Special Support Program (2021-527-07), the Leading Talent Project of the National Special Support Program (2022WRLJ003), and the Guangdong Basic and Applied Basic Research Foundation for Distinguished

Please cite this article in press as: S. Tian et al., Materials Today, (2023), https://doi.org/10.1016/j.mattod.2023.07.001

Young Scholars (Grant No. 2022B1515020070 and 2021B1515020083).

Appendix A. Supplementary material

Supplementary data to this article can be found online at https://doi.org/10.1016/j.mattod.2023.07.001.

References

[1] Z.L. Wang, J. Song, Science 312 (5771) (2006) 242–246.
[2] P. Horcajada et al., Nat. Mater. 9 (2) (2010) 172–178.
[3] Z.L. Wang, Adv. Mater. 24 (34) (2012) 4632–4646.
[4] W. Wu, Z.L. Wang, Nat Rev Mater 1 (7) (2016) 1–17.
[5] W. Wu et al., Nature 514 (7523) (2014) 470–474.
[6] W. Wu et al., Science 340 (6135) (2013) 952–957.
[7] C. Pan et al., Nat Photonics 7 (9) (2013) 752–758.
[8] J. Zhou et al., Nano Lett 8 (9) (2008) 3035–3040.
[9] B.W. Baugher et al., Nat Nanotechnol 9 (4) (2014) 262–267.
[10] A. Pospischil et al., Nat Nanotechnol 9 (4) (2014) 257–261.
[11] Y. Dai et al., Acs Nano 11 (7) (2017) 7118–7125.
[12] C.-H. Lee et al., Nat Nanotechnol 9 (9) (2014) 676–681.
[13] W. Peng et al., Adv. Mater. 29 (23) (2017) 1606698.
[14] X. Wang et al., Adv. Mater. 27 (14) (2015) 2324–2331.
[15] R. Bao et al., Adv. Funct. Mater. 25 (19) (2015) 2884–2891.
[16] Z. Pan et al., Nano Energy 49 (2018) 529–537.
[17] G. Hu et al., Nano Energy 23 (2016) 27–33.
[18] Y. Dai et al., Adv Sci 6 (16) (2019) 1900314.
[19] K.J. Lee et al., Acs Energy Lett 5 (10) (2020) 3295–3303.
[20] V. Kumaresan et al., Nano Lett 16 (8) (2016) 4895–4902.
[21] N. Syed et al., Acs Nano 16 (4) (2022) 5476–5486.
[22] Y. Dai et al., Adv. Mater. 30 (9) (2018) 1705893.
[23] K.M. Cho et al., Acs Catal 7 (10) (2017) 7064–7069.
[24] J.K. Utterback et al., Nat Chem 8 (11) (2016) 1061–1066.
[25] Z.-H. Zhao, Y. Dai, Phys Chem Chem Phys 21 (18) (2019) 9574–9580.
[26] L. Wang, Z.L. Wang, Nano Today 37 (2021) 101108.
[27] Y. Hu et al., Acs Nano 4 (2) (2010) 1234–1240.
[28] Q. Yang et al., Nano Lett 11 (9) (2011) 4012–4017.
[29] Q. Yang et al., Acs Nano 4 (10) (2010) 6285–6291.
[30] Z. Wang et al., Nat. Commun. 6 (1) (2015) 1–7.
[31] Z. Wang et al., Adv. Mater. 28 (32) (2016) 6880–6886.
[32] X. Han et al., J Mater Chem C 4 (48) (2016) 11341–11354.
[33] V. Panwar et al., J Mater Chem C 10 (35) (2022) 12487–12510.
[34] Y. Dai et al., Nano Energy 44 (2018) 311–318.
[35] X. Wang et al., Acs Nano 11 (8) (2017) 8339–8345.
[36] B. Dai et al., Chem. Soc. Rev. 50 (24) (2021) 13646–13691.
[37] X. Dai et al., J. Appl. Phys. 131 (1) (2022) 010903.
[38] C. Pan et al., Chem. Rev. 119 (15) (2019) 9303–9359.
[39] Z.L. Wang et al., Mat. Sci. Eng. R. 70 (3–6) (2010) 320–329.
[40] X. Hu et al., Adv. Funct. Mater. 31 (24) (2021) 2011284.
[41] W. Ouyang et al., Appl. Phys. Rev. 8 (3) (2021) 031315.
[42] C. Du et al., Adv Eng Mater 20 (5) (2018) 1700760.
[43] Y. Zhou et al., Nano Energy 101 (2022) 107586.
[44] S. Jeong et al., Acs. Appl. Mater. Inter. 10 (34) (2018) 28736–28744.
[45] D.Q. Zheng et al., Nano Energy 32 (2017) 448–453.
[46] Z.L. Wang et al., Mrs Bull 43 (12) (2018) 922–927.
[47] Z.L. Wang, Adv. Funct. Mater. 18 (22) (2008) 3553–3567.
[48] H. Li et al., J PHYS CHEM LETT 6 (17) (2015) 3410–3416.
[49] P. Wan et al., Adv Opt Mater 10 (2) (2022) 2101851.
[50] H. Li et al., Nano Energy 102 (2022) 107657.
[51] C.K. Jeong et al., Adv. Funct. Mater. 24 (18) (2014) 2620–2629.
[52] K. Momeni et al., J. Appl. Phys. 108 (11) (2010) 114303.
[53] L.J. Brillson, Y. Lu, J. Appl. Phys. 109 (12) (2011) 8.
[54] Z.-M. Liao et al., Phys. Lett. A 367 (3) (2007) 207–210.
[55] X. Wang et al., Nano Lett 17 (6) (2017) 3718–3724.
[56] M. Asif Khan et al., Appl. Phys. Lett. 63 (18) (1993) 2455–2456.
[57] H. Ferhati et al., Ieee Sens J 20 (7) (2019) 3512–3519.
[58] Y. Zhang et al., Acs. Appl. Mater. Inter. 14 (19) (2022) 22313–22323.
[59] Y. Wu et al., Chem Eng J 439 (2022) 135640.
[60] X. Wang et al., Adv. Mater. 28 (33) (2016) 7234–7242.
[61] W. Peng et al., Nano Res 9 (12) (2016) 3695–3704.
[62] Z. Wang et al., Acs Nano 8 (12) (2014) 12866–12873.
[63] R. Frisenda et al., Chem. Soc. Rev. 47 (9) (2018) 3339–3358.
[64] K. He et al., Angew Chem Int Edit 58 (34) (2019) 11903–11909.
[65] T. Yang et al., Nat. Commun. 8 (1) (2017) 1–9.
[66] S.M. Sze et al., Physics of semiconductor devices, John wiley & sons:, 2021.
[67] L. Huang et al., Nano Res 7 (2) (2014) 228–235.
[68] X. Xie et al., Nanoscale 4 (9) (2012) 2914–2919.
[69] X. Wang et al., J. Appl. Phys. 125 (9) (2019) 094505.
[70] N. Guo et al., Adv. Mater. 26 (48) (2014) 8203–8209.
[71] M. Shafa et al., Mater Lett 169 (2016) 77–81.
[72] S. Liu et al., J Mater Sci-Mater El 28 (13) (2017) 9403–9409.
[73] G. Li et al., Small 12 (36) (2016) 5019–5026.
[74] X.-X. Yu et al., J Mater Chem C 6 (3) (2018) 630–636.
[75] B. Tian et al., Chem. Soc. Rev. 38 (1) (2009) 16–24.
[76] M. Law et al., Nat. Mater. 4 (6) (2005) 455–459.
[77] J. Wallentin et al., Science 339 (6123) (2013) 1057–1060.
[78] M. Yao et al., Nano Lett 14 (6) (2014) 3293–3303.
[79] F. Boxberg et al., Nano Lett 10 (4) (2010) 1108–1112.
[80] C. Pan et al., Nano Lett 12 (6) (2012) 3302–3307.
[81] Y. Zhang et al., Nano Lett 7 (5) (2007) 1264–1269.
[82] J. Schrier et al., Nano Lett 7 (8) (2007) 2377–2382.
[83] K. Wang et al., Adv. Mater. 20 (17) (2008) 3248–3253.
[84] K. Wang et al., Appl. Phys. Lett. 96 (12) (2010) 123105.
[85] Z. Wu et al., J Mater Chem 21 (16) (2011) 6020–6026.
[86] F. Zhang et al., Acs Nano 6 (10) (2012) 9229–9236.
[87] X. Du et al., Nano energy 92 (2022) 106694.
[88] K. Wang et al., Nanoscale 6 (7) (2014) 3679–3685.
[89] S.C. Rai et al., Adv. Electron. Mater. 1 (4) (2015) 1400050.
[90] J. Luo et al., Acs Photonics 7 (6) (2020) 1461–1467.
[91] M. Dang et al., Appl. Phys. Lett. 110 (25) (2017) 253104.
[92] H. Zou et al., Acs Nano 13 (2) (2019) 2289–2297.
[93] Z. Huo et al., Nano Energy 86 (2021) 106090.
[94] M. Ahmadi et al., Adv. Mater. 29 (41) (2017) 1605242.
[95] G. Long et al., Nat Rev Mater 5 (6) (2020) 423–439.
[96] F. Zhang et al., Energy Environ. Sci. 13 (4) (2020) 1154–1186.
[97] X. Wang et al., Adv. Funct. Mater. 23 (9) (2013) 1202–1209.
[98] L.E. Greene et al., J. Phys. Chem. C 111 (50) (2007) 18451–18456.
[99] K. Zhang et al., Acs Nano 10 (11) (2016) 10331–10338.
[100] X.-X. Yu et al., Nano Energy 34 (2017) 155–163.
[101] P. Gao et al., J. Hazard Mater. 250 (2013) 412–420.
[102] D. Wang et al., Sci. Bull. 65 (2) (2020) 113–122.
[103] M. Shkir et al., Sens. Actuator A Phys. 301 (2020) 111749.
[104] K. Deng, L. Li, Adv. Mater. 26 (17) (2014) 2619–2635.
[105] M. Kumar et al., Nanoscale 9 (48) (2017) 19201–19208.
[106] Y. Zhang et al., Nano Energy 71 (2020) 104630.
[107] B. Yin et al., Nanoscale 9 (44) (2017) 17199–17206.
[108] Q. Li et al., Int. J. Optomechatroni 16 (1) (2022) 1–17.
[109] D. Gogoi et al., J. Mater. Chem. C 8 (19) (2020) 6450–6460.
[110] K. Zhao et al., Nano Energy 77 (2020) 105152.
[111] W. Zhao et al., Nano Energy 73 (2020) 104783.
[112] D. You et al., Nano Energy 62 (2019) 310–318.
[113] G. Yu et al., Nat. Commun. 10 (1) (2019) 1–8.
[114] X. Chen et al., Acs Nano 6 (3) (2012) 2550–2557.
[115] A.O. Govorov, H.H. Richardson, Nano today 2 (1) (2007) 30–38.
[116] Z. Yang et al., Nano Energy 85 (2021) 105951.
[117] Z. He et al., Mater. Today 62 (2022) 168–189.
[118] Q. Li et al., Adv. Funct. Mater. 32 (7) (2022) 2108903.
[119] K. Zhao et al., Iscience 3 (2018) 208–216.
[120] L. Guo et al., Nano Lett 22 (20) (2022) 8241–8249.
[121] L. Guo et al., Acs Nano 16 (1) (2022) 1280–1290.
[122] W. Ji et al., Adv. Mater. 22 (15) (2010) 1763–1766.
[123] T. Yang et al., Acs. Appl. Mater. Inter. 11 (26) (2019) 23372–23381.
[124] L. Wang et al., Appl. Phys. Lett. 102 (25) (2013) 252907.
[125] D. Li et al., Acs. Appl. Mater. Inter. 10 (23) (2018) 19836–19843.
[126] Y. Sun et al., InfoMat 1 (4) (2019) 496–524.
[127] L. Zheng et al., Adv. Funct. Mater. 30 (24) (2020) 2001604.
[128] Y. Zhang et al., Adv. Funct. Mater. 30 (5) (2020) 1907650.
[129] X. Cheng et al., Adv Mater Interfaces 3 (19) (2016) 1600485.
[130] A. Pescaglini et al., Nano Lett 14 (11) (2014) 6202–6209.
[131] Y. Zhang et al., Nano Energy 85 (2021) 105968.
[132] P.V. More et al., Sustain Energ Fuels 1 (8) (2017) 1766–1773.
[133] D. Dadarlat et al., Int. J. Thermophys. 37 (5) (2016) 1–7.
[134] S. Liu et al., Nano Energy 93 (2022) 106812.
[135] Y. Ding et al., Nat. Commun. 10 (1) (2019) 1–7.

Please cite this article in press as: S. Tian et al., Materials Today, (2023), https://doi.org/10.1016/j.mattod.2023.07.001

[136] C. Xiao et al., J. Am. Chem. Soc. 134 (9) (2012) 4287–4293.
[137] P. Jood et al., J Mater Chem A 8 (26) (2020) 13024–13037.
[138] W.Y. Lee et al., Adv Opt Mater 7 (22) (2019) 1900812.
[139] S. You et al., Nano Res 14 (10) (2021) 3386–3394.
[140] M. Park et al., Acs Photonics 5 (5) (2018) 1907–1911.
[141] W. Wang et al., InfoMat 2 (4) (2020) 761–768.
[142] K. Liu et al., Nano Lett 19 (11) (2019) 8132–8137.
[143] J. Ma et al., Acs Photonics (2022).
[144] Z. Xu et al., J Phys D Appl Phys 52 (22) (2019) 223001.
[145] F. Cao et al., Adv. Mater. 31 (12) (2019) 1806725.
[146] Q. Li et al., Adv Opt Mater 10 (7) (2022) 2102468.
[147] L. Zhu et al., Nano Res 11 (7) (2018) 3877–3885.
[148] L. Guo et al., Nano Lett (2022).
[149] Z. Yang et al., Small 17 (32) (2021) 2101572.
[150] J. Nie et al., J. Mater. Chem. C 8 (8) (2020) 2709–2718.
[151] H. Zhang et al., J. Mater. Chem. C 10 (33) (2022) 11903–11913.

Please cite this article in press as: S. Tian et al., Materials Today, (2023), https://doi.org/10.1016/j.mattod.2023.07.001